

An idealized LES study of urban modification of moist convection

Xiaoliang Zhu,^{a,b} Dan Li,^b Wenyu Zhou,^c Guangheng Ni,^a Zhentao Cong^a and Ting Sun^{a,d*}

^aDepartment of Hydraulic Engineering, State Key Laboratory of Hydro-Science and Engineering, Tsinghua University, Beijing, China

^bDepartment of Earth and Environment, Boston University, MA, USA

^cScripps Institution of Oceanography, University of California San Diego, La Jolla, CA, USA

^dDepartment of Meteorology, University of Reading, UK

*Correspondence to: T. Sun, Department of Hydraulic Engineering, State Key Laboratory of Hydro-Science and Engineering, Tsinghua University, Beijing 100084, China. E-mail: sunting@tsinghua.edu.cn

To understand the impacts of urbanization on moist convection, we explore how an idealized circular urban island affects the diurnal cycle and spatial distribution of rainfall over urban and surrounding rural areas at the diurnal equilibrium state using large-eddy simulations (LES) performed with the Weather Research and Forecasting (WRF) model. Compared to the control case where the whole domain is covered by grassland, the existence of an urban island significantly enhances the rainfall rate over the urban area as the stronger surface heating creates convergence zones and stronger vertical motions over the urban area. A suite of experiments is then conducted to investigate the effects of soil moisture of the surrounding rural land and the urban size on precipitation. Results show that as the rural soil moisture increases, both urban and rural precipitation rates increase almost linearly. This increase is not attributed to the urban heat island (UHI) effect but rather a stronger moisture deficit effect in the urban area creating a stronger moisture inflow. When the urban area becomes larger but the initial available water remains the same in the domain, the UHI effect and moisture deficit effect increase but the total water supply decreases. As a result, the urban rainfall rate increases first and then decreases as the urban size increases. This suggests that there is an 'optimal' scale at which the urban rainfall rate is maximized, at least in our modelling framework. Our simulations further suggest that this optimal scale occurs when the urban fraction lies between 1 and 10%.

Key Words: large-eddy simulation; moist convection; precipitation; urban heat island

Received 2 April 2017; Revised 18 August 2017; Accepted 4 October 2017; Published online in Wiley Online Library

1. Introduction

With more than 50% of the global population now living in cities and continued urbanization, cities are becoming the nexus of water, energy and health challenges facing humanity in the twenty-first century (Grimm *et al.*, 2008; United Nations, 2014). The continuous growth of urban population and the changing global climate mandate a better understanding of urban–atmosphere interactions within the context of climate change and variability. In response to this need, many studies have focused on the impact of urbanization on temperature, namely, the urban heat island effect (Oke, 1982; Arnfield, 2003). The factors contributing to the urban heat island (UHI) effect are relatively well understood nowadays, including reduced evapotranspiration due to abundant impervious surfaces, enhanced heat storage during daytime which is released at night-time, and anthropogenic heat fluxes (Oke, 1982; Grimmond, 2007; Nie *et al.*, 2014). However, the hydrometeorological impacts of urbanization remain elusive (Lowry, 1998; Shepherd, 2005; Mahmood *et al.*, 2014).

The major challenges limiting our understanding of urban modification of convection is the difficulty in separating the

urban signature from those of topography, land–sea or land–lake boundaries, and the large-scale atmospheric forcing in field experiments or in real-case modelling studies. As a result, studies conducted at different locations, in different seasons, and/or under different synoptic conditions often produce different findings. For example, the traditional paradigm generated by the famous METROpolitan Meteorological EXperiment (METROMEX) in the early 1970s (Changnon *et al.*, 1971; Changnon, 1981) suggests that the precipitation rate in the downwind region of urban areas increases due to the enhanced vertical motion in urban areas. However, a recent modelling study by Schmid and Niyogi (2013) documented that, in weak convection cases, urban regions can either suppress or invigorate rainfall over the downwind area. Trusilova *et al.* (2008) studied the impact of urbanization in Europe and found that replacing urban areas by grassland in a numerical model increases the rainfall amount in winter by an average value of 0.09 mm day⁻¹ but reduces the rainfall amount in summer by an average value of -0.05 mm day⁻¹. Lei *et al.* (2008) simulated the 26 July 2005 heavy rainfall event over Mumbai, India and found that the city had a significant impact on the vertical wind structure, with

Table 1. Simulation characteristics.

Domain sizes	20 km (x), 20 km (y), 10 km (z)
Resolutions	100 m (x), 100 m (y), 100 levels (z)
Time step	1 s, third-order Runge–Kutta scheme
Simulation duration	30 days
Microphysical scheme	WSM 6-class graupel
Eddy coefficient option	1.5-order TKE closure
Long-wave scheme	Rapid radiative transfer model
Short-wave scheme	Dudhia scheme (38°N at 3 July)
Surface layer scheme	MM5 Monin–Obukhov scheme
Land surface model scheme	Noah land surface model with single layer urban canopy model

Table 2. An overview of the experiment cases.

Case name	Feature ISM ($\text{m}^3 \text{m}^{-3}$)	Case name	Feature	
			D (km)	ISM ($\text{m}^3 \text{m}^{-3}$)
S0.2	0.2	D2.5	2.5	0.242
S0.25	0.25	D5/D5L	5	0.25
S0.3	0.3	D7.5	7.5	0.265
S0.35	0.35	D10	10	0.290

ISM means the initial soil moisture and D means the diameter of the city. D5L means the case with an urban diameter of 5 km urban area in the larger domain (40 km \times 40 km).

more precipitation occurring in the upwind region of Mumbai. However, Yang *et al.* (2014) investigated the 22–23 July 2010 heavy convective precipitation event in the Milwaukee, Wisconsin metropolitan region and concluded that urbanization had little effect on the vertical dynamics of the precipitating cloud system. Many other similar studies have been conducted around the world as reviewed elsewhere (Shepherd, 2005; Pielke *et al.*, 2011; Mahmood *et al.*, 2014; Zhang *et al.*, 2014b; Yeung *et al.*, 2015; Nie *et al.*, 2017). All of these studies suggested strong connections between urban areas, convection enhancement, and increased precipitation. However, these experimental and modelling studies were unable to elucidate the fundamental mechanisms and pathways due to their consideration of all features in a fully interactive way.

Inspired by idealized modelling studies (Schlemmer *et al.*, 2011, 2012; Schmid and Niyogi, 2013) and the widely used large-eddy simulation (LES) technique (Moeng *et al.*, 2007; Reinert and Wirth, 2009; Talbot *et al.*, 2012; Yamaguchi and Feingold, 2012), we propose to use LES to perform controlled and quasi-idealized simulations to unravel the fundamental mechanisms through which urban surfaces initialize and modulate moist convection. The use of LES avoids the uncertainties from cumulus parametrizations by explicitly resolving moist convection and from planetary boundary layer (PBL) parametrizations by explicitly resolving large turbulent eddies, respectively. As a logical starting point, we focus on the impacts of urban/rural characteristics and contrasts but do not consider the effects of large-scale forcing, topography and land–water boundaries. These complexities will be gradually and systematically added to the modelling system in forthcoming studies, thereby enabling a qualitative and quantitative understanding of interactions between urban/rural characteristics and other complexities in affecting moist convection.

Based on the idealized large-eddy simulations framework, we will also investigate how the effect of an urban island on moist convection is modulated by different soil moisture conditions in the surrounding rural areas. This is motivated by the rich literature on soil moisture–precipitation coupling, which has been debated in terms of positive feedback or negative feedback between soil moisture and precipitation (Betts *et al.*, 1996; Eltahir, 1998; Hohenegger *et al.*, 2009; Seneviratne *et al.*, 2010; Taylor *et al.*, 2012; Guillod *et al.*, 2015; Tuttle and Salvucci, 2016). A recent study (Tuttle and Salvucci, 2016) presented empirical evidence

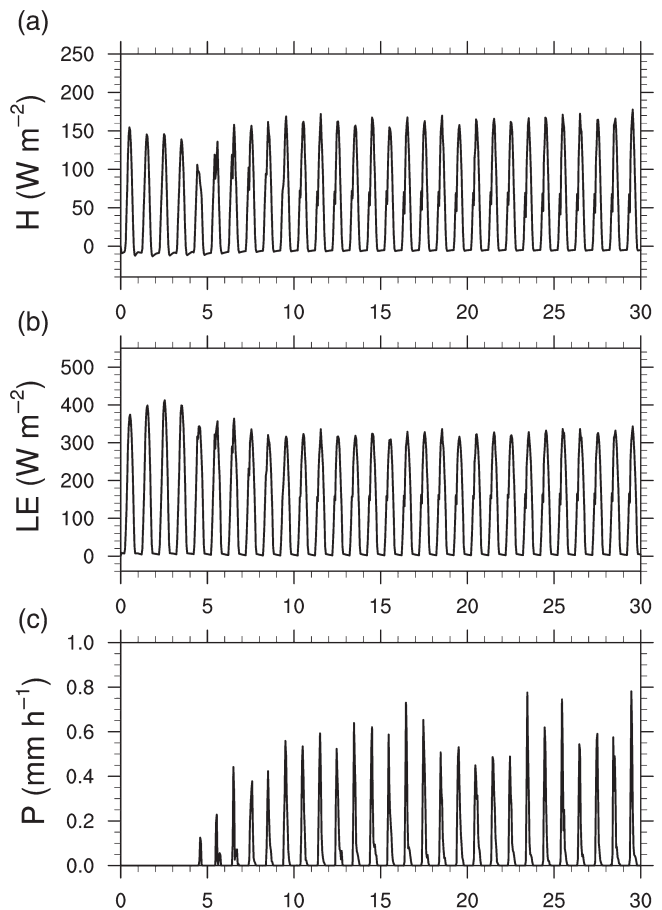


Figure 1. The temporal evolution (days) of domain-averaged (a) sensible heat flux H (W m^{-2}), (b) latent heat flux LE (W m^{-2}), and (c) surface rainfall rate P (mm h^{-1}).

of contrasting soil moisture–precipitation feedbacks across the United States and showed that the feedback is generally positive in the west and negative in the east, indicating the important role of regional aridity. This suggests that the background climate (thus the large-scale rural conditions in which cities are located) might play a role in the problem of urban modification of rainfall. In addition, another recent study by Guillod *et al.* (2015) showed that afternoon rainfall occurs preferentially over wetter areas in the mean sense but over drier areas if the terrain is heterogeneous. Their findings were based on remote-sensing data and have not been validated using process-based models. Our idealized LES modelling framework avoids the uncertainty from moist parametrization by explicitly resolving moist convection, and thus will be very useful for evaluating these results.

Besides the rural soil moisture, the influence of urban size is also investigated, which has important implications for understanding the impacts of further urban growth on the local climate. Many previous studies have examined this issue but by simulating real-world cases. For example, Shepherd *et al.* (2010) found expanded areas of rainfall with the 2025 land-cover scenario in Houston. Schmid and Niyogi (2013) studied the magnitude of precipitation-modification potential of cities of different sizes under a particular synoptic condition and concluded that modification of rainfall increases linearly with the city size but such an increase becomes much slower when the city size is larger than 20 km. However, this seems to be inconsistent with a recent radiative–convective equilibrium study on precipitation over tropical islands where precipitation over an island was found to increase with the size of the island when the radius of the island is smaller than 20 km in a domain of 400 km by 400 km. Once the island radius becomes larger than 20 km, the precipitation starts to decrease (Cronin *et al.*, 2015). The Weather Research and Forecasting WRF-LES model introduced here is different from the models used in the studies just mentioned and hence is used to revisit this issue. It

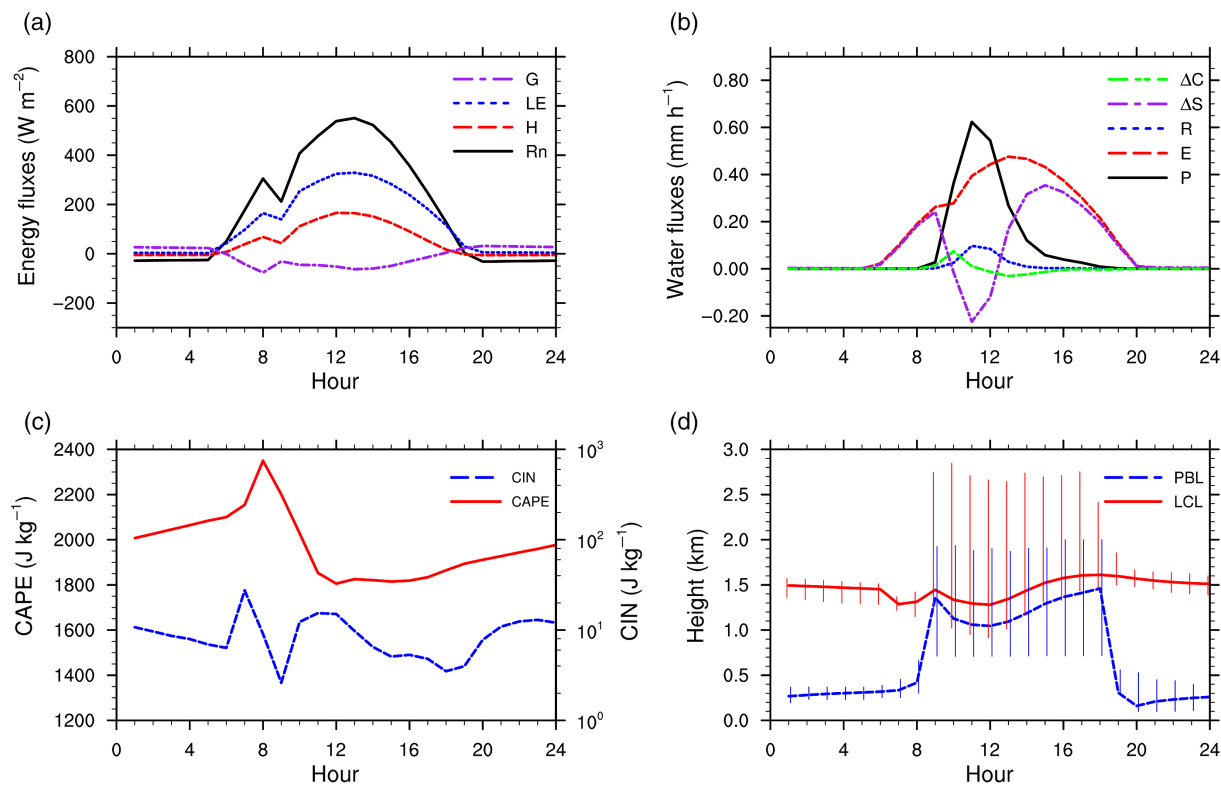


Figure 2. The average diurnal cycles of (a) energy fluxes: surface net radiation (Rn, black line), surface sensible heat flux (H, red), surface latent heat flux (LE, blue) and ground heat flux (G, purple, positive towards up) (W m^{-2}); (b) water fluxes: surface precipitation rate (P, black), surface evapotranspiration (E, red), surface runoff (R, blue), the change of soil moisture (ΔS , purple) and the change of canopy water (ΔC , green) (mm h^{-1}); (c) convective available potential energy CAPE and convective inhibition CIN (J kg^{-1}); (d) the domain-average height of lifted condensation level LCL (solid) and planetary boundary layer PBL (dashed) (km). The vertical bars in (d) indicate the range of LCL and PBL. [Colour figure can be viewed at wileyonlinelibrary.com].

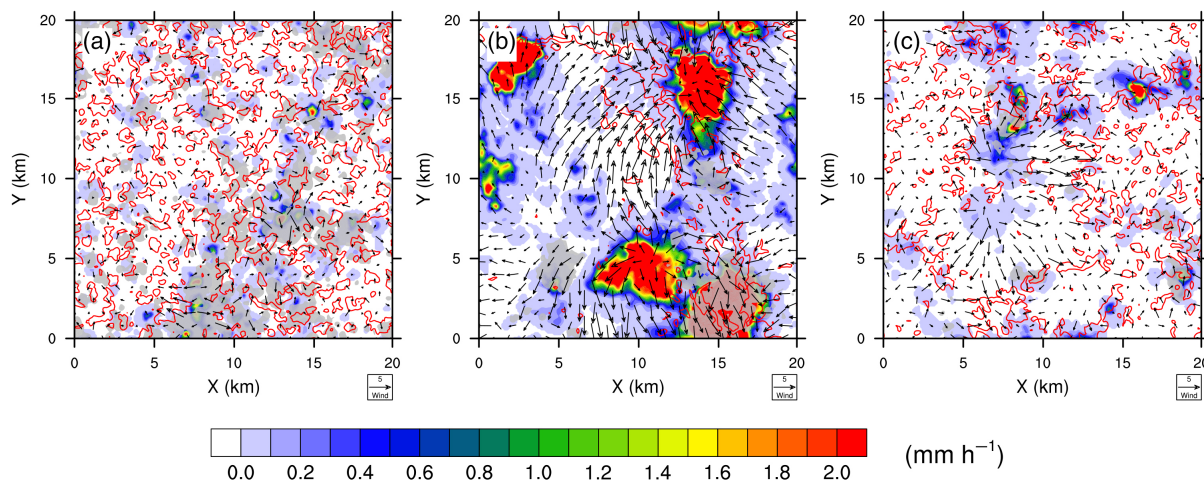


Figure 3. Spatial distributions of wind, cloud, and precipitation at (a) 0900, (b) 1100 and (c) 1700 LST. The coloured shading indicates the precipitation (mm h^{-1}). The grey shading is the cloud water mixing ratio where the column-integrated values larger than 0.01 g kg^{-1} are displayed. The red contour lines indicate upward velocity larger than 1.0 m s^{-1} at 700 m, and the black arrows are horizontal winds at 160 m. [Colour figure can be viewed at wileyonlinelibrary.com].

is noted that the problem considered here is more complicated than the problem of rainfall enhancement over tropical islands because the surrounding rural land in our configuration, unlike the ocean, does not have an unlimited water supply.

The article is organized as follows: section 2 describes the configuration of the model and numerical experiments; section 3 analyses and discusses the simulation results; section 4 presents the conclusions of our study.

2. Method

2.1. Model description and configuration

The numerical experiments are performed with the WRF-LES model (Moeng *et al.*, 2007; Talbot *et al.*, 2012; Yamaguchi and Feingold, 2012). The WRF model is a non-hydrostatic model

based on fully compressible Euler equations. It has proven to be a useful simulation tool to investigate convective PBL characteristics under heterogeneous heating conditions (Liu *et al.*, 2011; Kang and Lenschow, 2014). In a previous study, we have made some necessary modifications in the WRF Version 3.5.1 to take into account the urban features (Zhu *et al.*, 2016).

In all the simulations, the model is initialized with idealized potential temperature and specific humidity profiles. The potential temperature is 300 K below 950 m , and there is a strong inversion layer of 50 K km^{-1} from 950 to 1050 m . Above 1050 m , the potential temperature has a gradient of 3 K km^{-1} . For the specific humidity, there is a slightly decreasing trend from 6.00 g kg^{-1} at the ground surface to 5.8 g kg^{-1} at 950 m and a jump at the inversion layer to 2.0 g kg^{-1} in all the free atmosphere levels. Potential temperature fields in the WRF-LES model are perturbed randomly at the first four vertical layers to break the symmetry

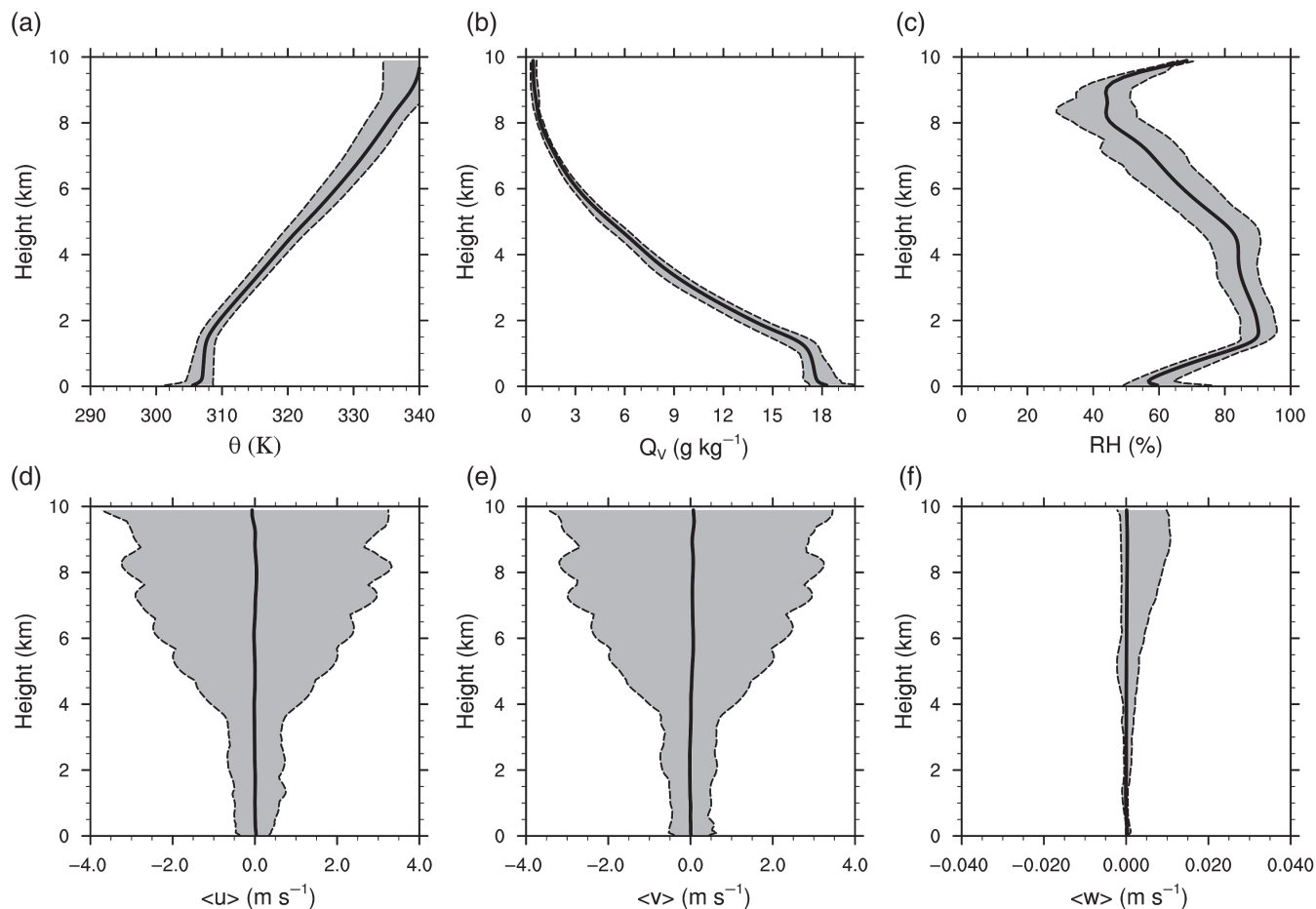


Figure 4. Profiles of (a) potential temperature (K), (b) water vapour mixing ratio (g kg^{-1}), (c) relative humidity (%), (d) longitudinal wind (m s^{-1}), (e) meridional wind (m s^{-1}) and (f) vertical wind (m s^{-1}). The black lines show the averaged profiles in the last 3 days, and the shadow areas show the range of hourly profiles.

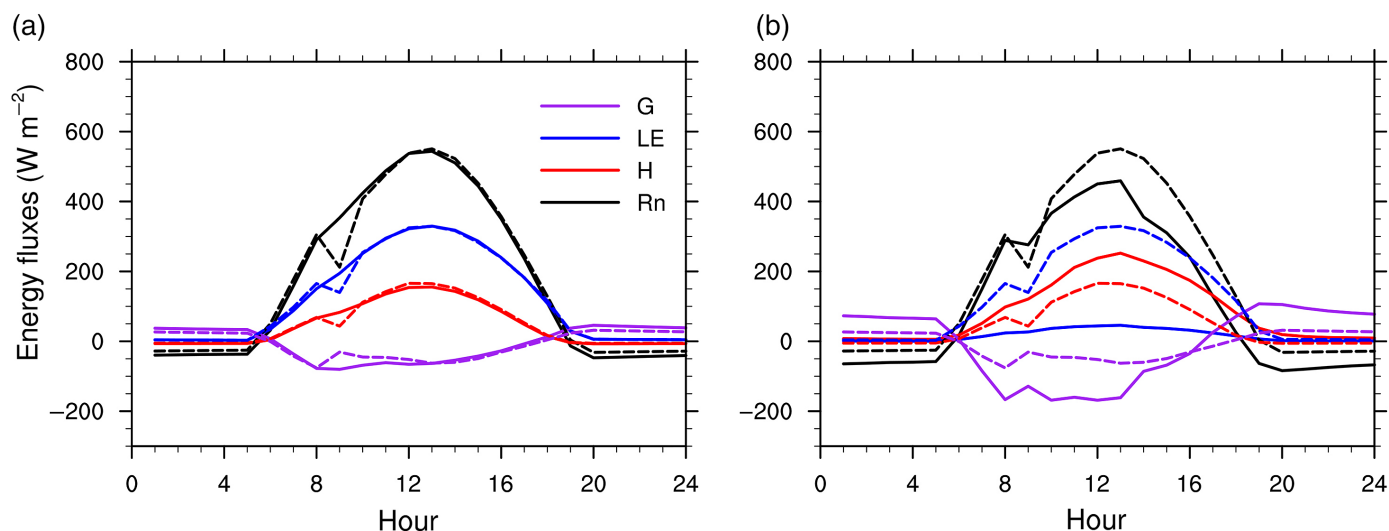


Figure 5. The averaged diurnal cycle of the surface energy balance: (a) average values over the whole domain; (b) average values over the urban area for case URB. The solid lines and dashed lines are the energy fluxes in the case URB and case CTL, respectively. [Colour figure can be viewed at wileyonlinelibrary.com].

of the initial conditions. The model is driven by periodic lateral boundary conditions in the horizontal directions and runs for a sufficiently long period to achieve diurnal equilibrium. Since no nudging is performed, the initial profiles should not have any impacts on the final results.

We use the unified Noah land-surface model with four soil levels (0.1, 0.3, 0.6 and 1 m) to predict soil temperature and soil moisture. A small change we have made is the treatment of runoff. Without treatment, the generated runoff leaves the simulation domain and never comes back. The amount of runoff is very small in our study due to the fact that no topography is considered, and has little effect on our simulated results. To conserve water in the

land surface, both surface runoff and subsurface runoff generated over the previous time step is redistributed into the first soil layer locally in the next time step. If the first layer is saturated, the remainder of the water will be distributed into the next layer and so on. However, it should be noted that we do not deal with the runoff generated over the impervious surface in the urban area.

As for other physical schemes in the WRF model, the 1.5-order turbulent kinetic energy scheme (Deardorff, 1980) is used to compute the subgrid-scale eddy viscosity and eddy diffusivity. The WRF Single-Moment (WSM) 6-class (Hong and Lim, 2006) microphysics scheme, which is suitable for high-resolution simulations and can also take account of ice,

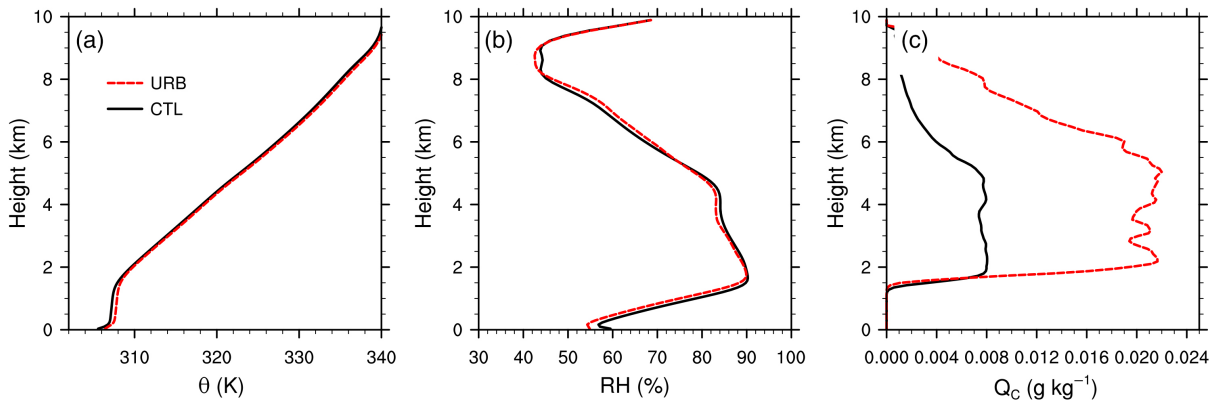


Figure 6. Vertical profiles for URB and CTL of (a) potential temperature (K), (b) relative humidity (%), and (c) cloud water mixing ratio ($g\ kg^{-1}$). The values of case URB (dashed red line) are averaged over the urban area. [Colour figure can be viewed at wileyonlinelibrary.com].

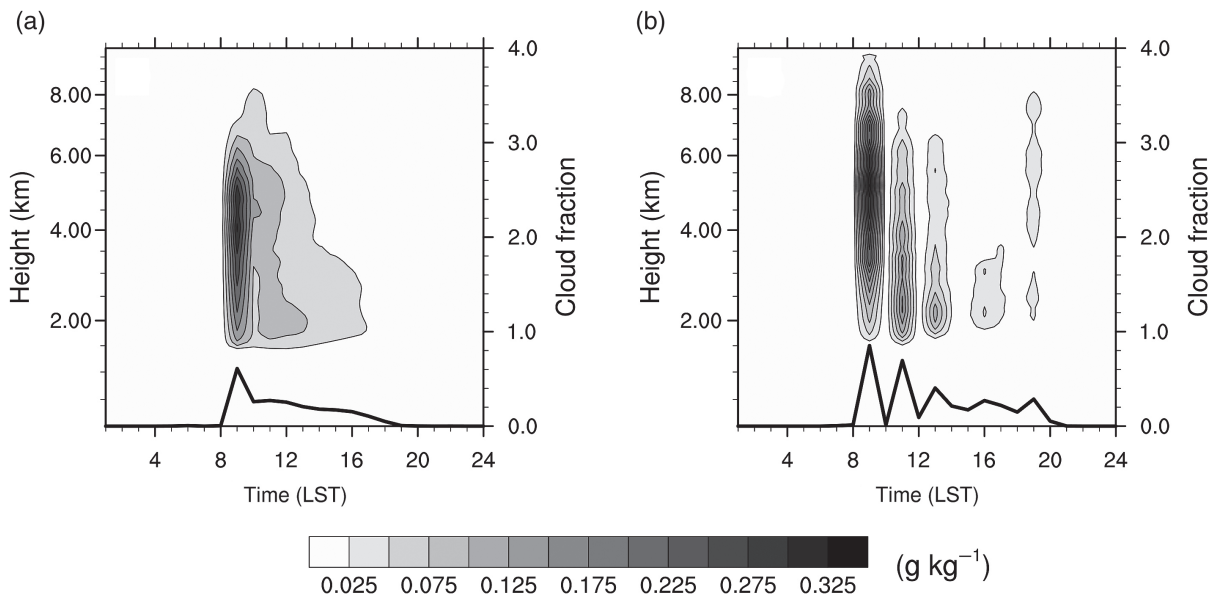


Figure 7. The diurnal cycles of cloud water mixing ratio ($g\ kg^{-1}$, shaded area) and cloud cover fraction (solid black line) for cases (a) CTL and (b) URB. The values of case URB are averaged over the urban area. Note that the y-axis is not equidistant as the WRF model uses eta levels in the vertical direction.

snow and graupel processes, is utilized. The Rapid Radiative Transfer Model scheme (RRTM: Mlawer *et al.*, 1997) and Dudhia scheme (Dudhia, 1989) are chosen as the long-wave radiation and the short-wave radiation scheme, respectively. The planetary boundary-layer parametrization scheme is turned off since we use the LES mode. The MM5 Monin–Obukhov scheme in the WRF

model, which is based on the Monin–Obukhov similarity theory (MOST), is chosen as the surface layer scheme to determine exchange coefficients. The geostrophic wind is set to zero in our study and its influence is left for future investigations. The surface in the whole simulation domain is flat and the influence of topography is also left for future studies.

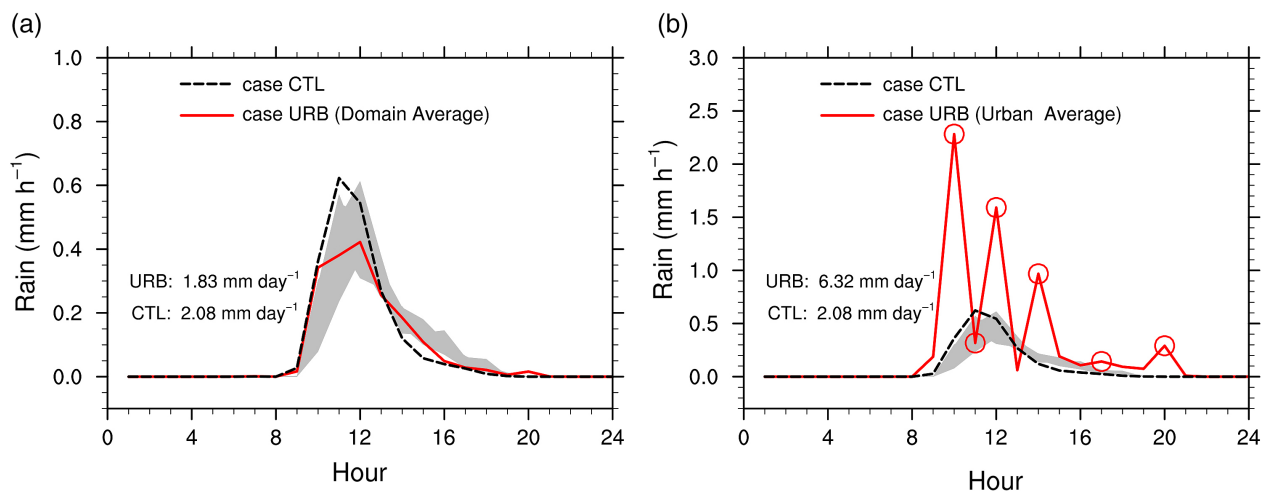


Figure 8. The diurnal cycles of the surface precipitation rate (a) averaged over the whole domain; (b) averaged over the urban area for case URB. Note the change in the range of y-axis between (a) and (b). The red solid lines and black dashed lines are the rainfall rate in the case URB and case CTL. The shaded area indicates the range of rainfall rates in sensitivity cases presented in the appendix. The red marker in (b) indicates the times at which horizontal distributions of surface precipitation are shown in Figure 9. [Colour figure can be viewed at wileyonlinelibrary.com].

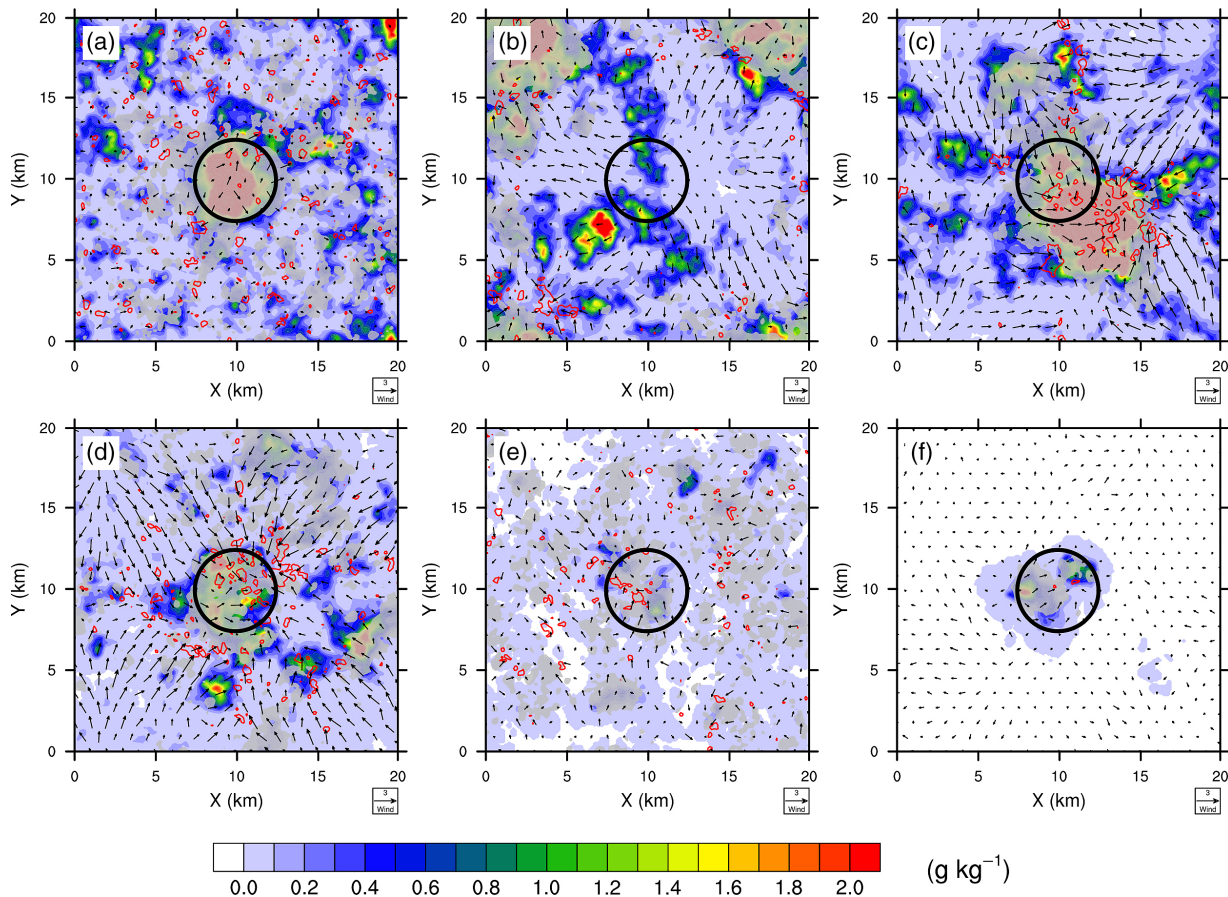


Figure 9. Same as Figure 3 but for case URB. (a), (b), (c), (d), (e) and (f) are results at 1000, 1100, 1200, 1400, 1700 and 2000 LST, respectively. These times are marked by red circles in Figure 8(b) accordingly. [Colour figure can be viewed at wileyonlinelibrary.com].

2.2. Numerical experiments

For all simulations, the domain size is $20 \text{ km} \times 20 \text{ km} \times 10 \text{ km}$ along the x , y and z directions and is centred at the latitude of 38°N . All simulations run for 30 days with a fixed diurnal cycle of incoming short-wave radiation at the top of the atmosphere (3 July 2013). The resolution in both x - and y -direction is 100 m, while the vertical grid spacing varies with height from 32 to 160 m. A time step of 1 s is used. In the control case (case CTL), the land surface is covered by homogeneous grassland with the initial soil moisture $0.25 \text{ (volumetric, m}^3 \text{ m}^{-3}\text{)}$. The simulation characteristics in case CTL is shown in Table 1. To study urban modification of moist convection, we perform case URB with the same domain size as the control case but with a circular urban island with a diameter of 5 km located in the centre of the domain. To parametrize urban land processes, the single-layer urban canopy model coupled into the Noah land surface model is turned on. The type of urban land in the cases URB is set to be high-intensity residential urban.

Besides the case URB, we also design several other cases shown in Table 2 to study the effects of soil moisture of the surrounding rural land and urban size. Cases starting with S (i.e. S0.2, S0.25, S0.3 and S0.35, where the number refers the initial soil moisture in units of $\text{m}^3 \text{ m}^{-3}$) are designed to study the effect of soil moisture. Meanwhile, the wilting point is $0.066 \text{ m}^3 \text{ m}^{-3}$ and the saturated value of soil moisture is $0.439 \text{ m}^3 \text{ m}^{-3}$ in our study. In these cases, an urban island with a fixed diameter of 5 km is located in the centre of the domain, and the soil moisture is uniformly prescribed across all layers. Cases starting with D (i.e. D2.5, D5, D7.5 and D10, where the number refers to the diameter of the circular city in units of km and the initial soil moisture is $0.25 \text{ m}^3 \text{ m}^{-3}$) are designed to study the effect of urban size. Due to the use of doubly periodic boundary conditions in our simulations, the urban areas are kept less than 20% of the domain to avoid the influence of upwind cities. To ensure

identical initially available water amounts in the domain as in case D5, the initial soil moisture (ISM) in cases D2.5, D7.5 and D10 is determined as:

$$\text{ISM} = \frac{\langle 0.25 \times (S_{\text{domain}} - S_{\text{urban}} \times \text{FRC}_{\text{imp}}) \rangle_{\text{D5}}}{\langle (S_{\text{domain}} - S_{\text{urban}} * \text{FRC}_{\text{imp}}) \rangle_{\text{D}}}, \quad (1)$$

where ISM is the initial soil moisture, S_{domain} is the domain area 400 km^2 , S_{urban} is the urban area and the FRC_{imp} is the impervious surface fraction in the urban grid (0.9 in our simulation). The angle brackets denote the value in different cases. Therefore, the initial soil moisture in cases D2.5, D7.5 and D10 are 0.242, 0.265 and 0.290, respectively. In addition, we also perform a case with an urban diameter of 5 km in a $40 \text{ km} \times 40 \text{ km}$ domain (case D5L).

Before the numerical experiments were conducted, we first did several sensitivity cases (without an urban island) to investigate the sensitivity to both spatial resolutions and physical schemes using simulations of 2 weeks long. In particular, we tested the performance of the Smagorinsky subgrid-scale scheme and the WSM 3-class microphysical scheme. To test the impact of the model resolution, we conducted three simulations with the horizontal resolution of 50 and 200 m, and 50 levels in the vertical direction, respectively. These sensitivity experiments are designed to understand the uncertainties in our CTL simulation and quantify the significance of the influence of urban areas. As they are not the central focus of our study, the results are presented in the appendix.

3. Results and discussion

3.1. Characteristics of the diurnal equilibrium in the control simulation

In this section, we describe the results of the control simulation with a homogenous grassland surface. Figures 1–4 show

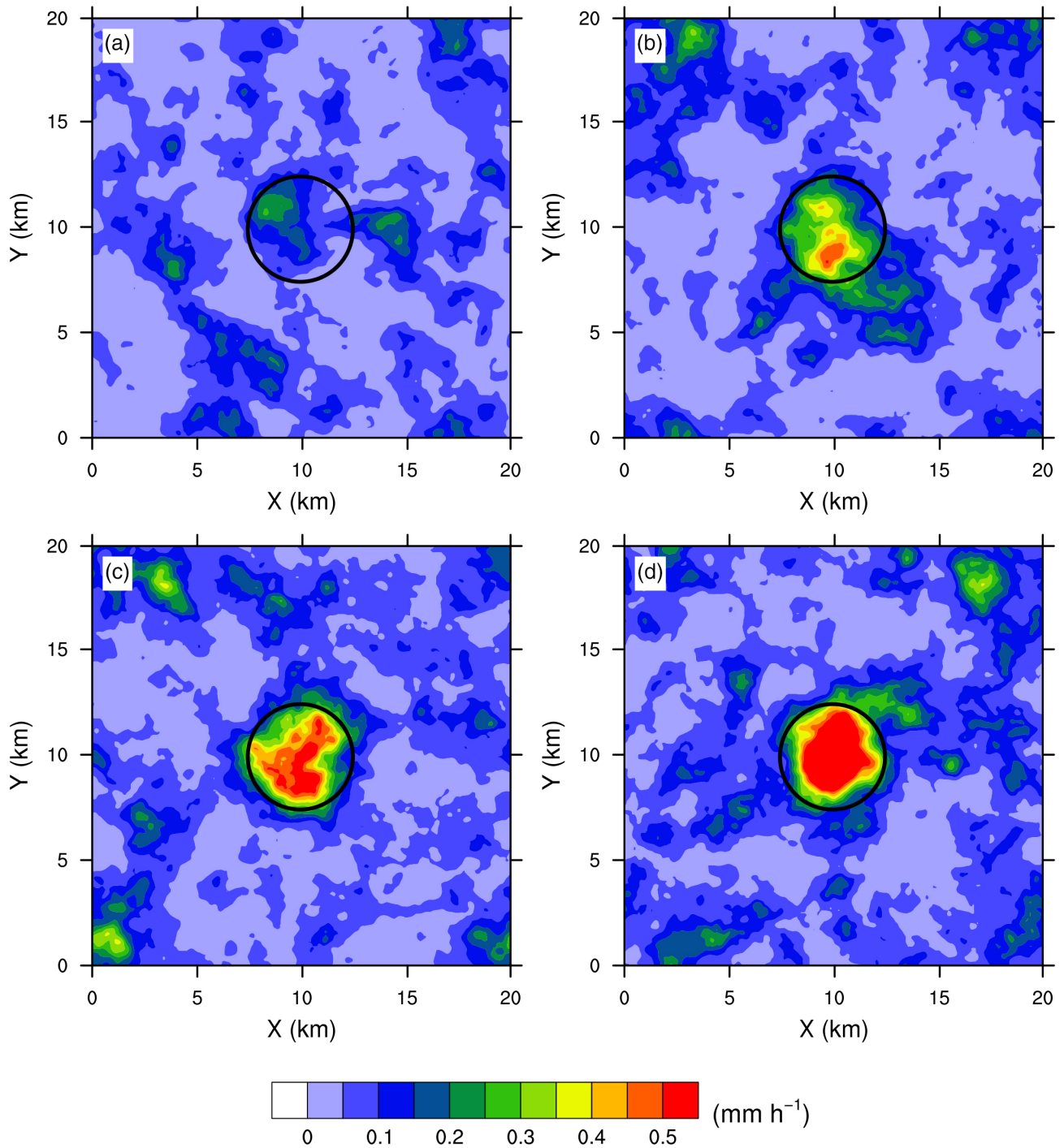


Figure 10. Surface precipitation rates (mm h^{-1}) averaged over the last 7 days from (a) case S0.2; (b) case S0.25; (c) case S0.3; and (d) case S0.35. The black circle denotes the urban area. [Colour figure can be viewed at wileyonlinelibrary.com].

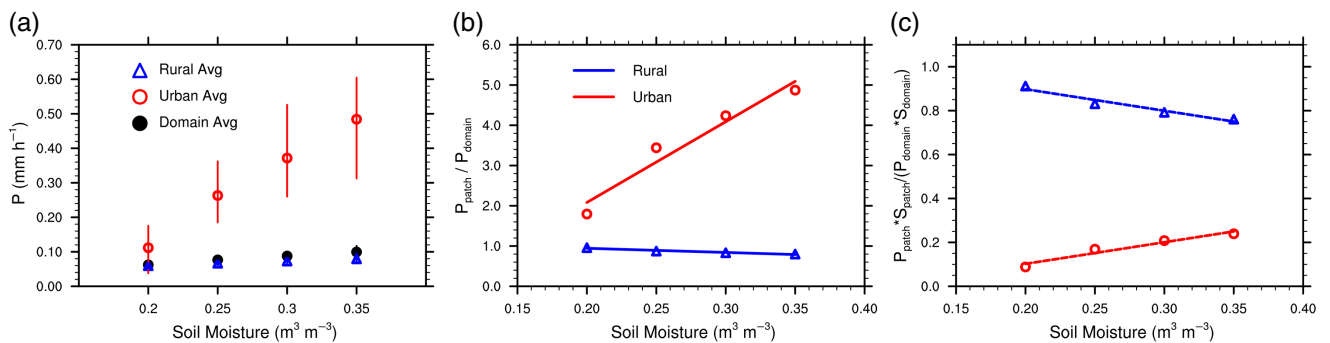


Figure 11. (a) The surface precipitation rates average over different regions, by soil moisture. (b) The urban/rural surface precipitation rates normalized by the domain-averaged precipitation rate. (c) The urban/rural total rainfall amount normalized by the total rainfall amount over the whole domain. The error bars in Figure 11(a) indicate the range of rainfall rates. [Colour figure can be viewed at wileyonlinelibrary.com].

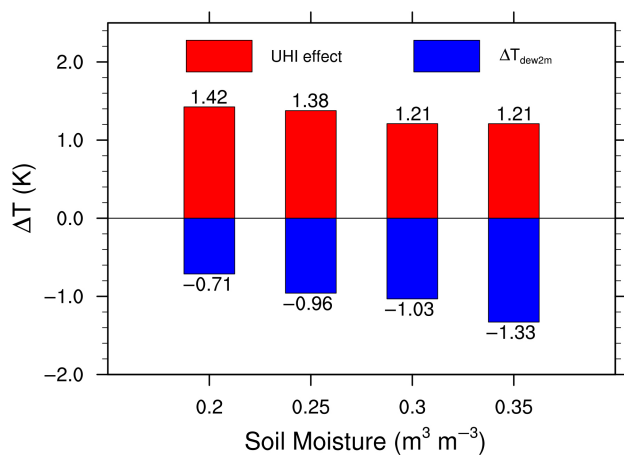


Figure 12. The average urban heat island effect (the difference in potential temperature at 2 m height) and moisture deficit effect (the difference in dew-point temperature at 2 m height), by soil moisture. [Colour figure can be viewed at wileyonlinelibrary.com].

the results of temporal evolution, diurnal cycles, horizontal distributions, and vertical profiles, respectively.

Figure 1 shows the temporal evolution of domain-averaged surface and atmospheric properties, including (a) sensible heat flux H , (b) latent heat flux LE , (c) surface rainfall rate P . It can be seen that the model gradually moves to a quasi-equilibrium state as the simulation develops and changes in daily averages of these variables become much slower and smaller (not shown). Turbulent heat fluxes (Figures 1(a) and (b)) and rainfall rate (Figure 1(c)) show clear diurnal cycles in the simulation. After the second week, the diurnal cycle of precipitation (Figure 1(c)) starts to repeat itself from day to day, suggesting the onset of diurnal equilibrium convection as found in previous studies (Schlemmer *et al.*, 2011, 2012), which is loosely defined as the repeating pattern from day to day. Note that the whole land–atmosphere system here has not reached true equilibrium due to the long memory of soil moisture (Koster and Suarez, 2001; Rochetin *et al.*, 2014). In the following, the average results from the last 7 days are used in this study hereafter if not otherwise stated.

We then examine the average diurnal cycles of surface energy (Figure 2(a)) and water balances (Figure 2(b)). The surface net radiation (Figure 2(a), black line, R_n) is apparently affected by clouds (see for example the dip of R_n around 0900 LST, local solar time). The Bowen ratio ranges from 0.16 at the beginning of the day to 0.51 at noon and its average value is about 0.4. These results are broadly consistent with observations over grasslands (Xu *et al.*, 2002). The rain begins at 0900 LST, peaks at 1100 LST and comes to an end at 1800 LST. For comparison, we define $\Delta s > 0$ as the reduction of soil moisture and it is clear from Figure 2(b) that before the rain starts evapotranspiration is balanced by the reduction of soil moisture. It is pointed out that a small amount of runoff is generated because sometimes the precipitation rate exceeds the infiltration capacity. To conserve the water, the generated runoff is captured and redistributed into the soil instead of allowing it to leave the simulation domain. We note that this has little effect on the averaged results. In addition, we notice that the Noah land surface model and WRF does not impose a strict stringency on water conservation, and a small water imbalance is observed especially when a small time step (like 1 s used here) is used.

The diurnal cycles of convective available potential energy (CAPE) and convective inhibition (CIN) are shown in Figure 2(c). CAPE reaches a peak exceeding 2350 J kg^{-1} at 0800 LST right before it starts to rain. Almost at the same time, CIN reaches its minimum value of about 0.5 J kg^{-1} at 0900 LST. Close inspection of the high-frequency (1 min) outputs reveals that the rain begins at 0840 LST. Figure 2(d) illustrates the diurnal cycles of the lifting condensation level (LCL) and the PBL height. We compare

these two variables because the PBL height exceeding the LCL is often viewed as a necessary condition for the onset of convective precipitation (Stull and Eloranta, 1984; Wilde *et al.*, 1985; Haiden, 1997; Findell and Eltahir, 2003; Juang *et al.*, 2007; Siqueira *et al.*, 2009; Kang and Bryan, 2011; Santanello *et al.*, 2011; Gentine *et al.*, 2013; Yin *et al.*, 2015). The PBL height is calculated using the potential temperature gradient method, where the thresholds for stable and unstable conditions are 1 and 2 K km^{-1} , respectively. As can be seen, although the domain-averaged PBL height is always lower than LCL, the spatial variability of PBL height and LCL, indicated by the error bars, is significant, implying overlaps between PBL height and LCL in parts of the domain that may be conducive for convection.

Figure 3 shows the spatial distributions of wind, cloud and precipitation right before (Figure 3(a)), during (Figure 3(b)), and after (Figure 3(c)) the intensive rainfall period in the last day of the simulation. It can be seen that the convergence zones accompany the updraught regions (red line loops) where the upward wind speed is larger than 1.0 m s^{-1} . Clouds mostly appear over these convergence areas, but precipitation only occurs adjacent to these convergence areas. At 0900 LST, the rain event is at its early stage with small rainfall rates. At 1100 LST, the convection is very strong covering a much larger area, and many organized updraughts appear. At 1700 LST, clouds and updraught regions are significantly reduced and little rain remains.

Figure 4 shows the domain-averaged vertical profiles of potential temperature, water vapour mixing ratio, relative humidity and winds. Distinct features of thermal (Figure 4(a)) and moist (Figures 4(a) and (b)) conditions are observed between the atmospheric boundary layer (the lower 1–2 km) and the free atmosphere (above 2 km). Over a diurnal course, the profiles of potential temperature and water vapour mixing ratio in the upper troposphere show minimal changes but those in the atmospheric boundary layer have apparent diurnal cycles (not shown). In the daytime, the surface heating destabilizes the atmospheric boundary layer and leads to convection. As there is no geostrophic wind in our simulation, the horizontal wind speeds are on average close to zero and their fluctuations are mainly controlled by the surface heating and cooling in daytime and night-time, respectively. Due to the use of periodic lateral boundary conditions, the vertical wind speed (Figure 4(f)) is always orders of magnitude smaller than the horizontal wind speeds (Figures 4(d) and (e)).

3.2. Impacts of the existence of an urban island

In this section, we present results from case URB, in which an urban island is created in the centre of the domain, to study the impact of an urban island on moist convection. First of all, we note that the domain-averaged diurnal cycles of the surface energy balance are similar between the default case and the case URB (Figure 5(a)), due to the small fraction of the urban island. However, it can be seen from Figure 5(b) that the energy fluxes averaged value over the urban island are very different from those in the case URB. The surface net radiation in the urban area is smaller than the domain-average value because of more rainfall and clouds over the urban area, which will be seen later. Even so, the sensible heat flux over urban areas in the case URB is much larger than the latent heat flux. This is because 90% of the urban island is impervious since the urban category is set to be high-density residential as mentioned earlier. The higher sensible heat flux over urban areas can result in urban–rural circulations and stronger vertical motions over urban areas (not shown here but see e.g. Kang and Lenschow (2014), Zhang *et al.* (2014a) and Zhu *et al.* (2016)), which facilitate cloud formation and moist convection.

Figure 6 shows the vertical profiles of potential temperature, relative humidity, and cloud water mixing ratio of case CTL and case URB. It can be seen that there is no significant difference of the daily average profiles in terms of potential temperature,

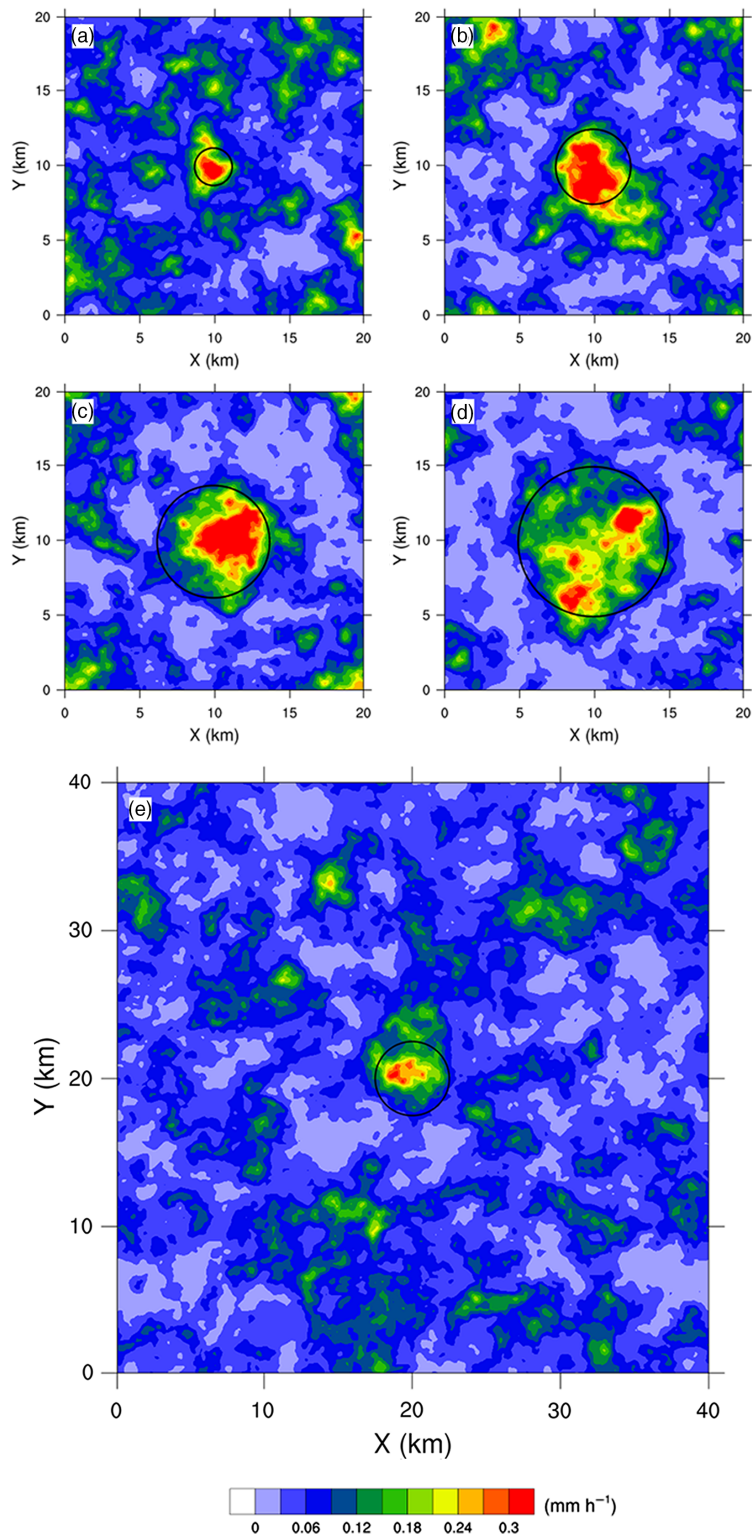


Figure 13. Same as Figure 10 but for (a) case D2.5, (b) case D5, (c) case D7.5, (d) case D10, and (e) case D5L. [Colour figure can be viewed at wileyonlinelibrary.com].

and relative humidity. The atmosphere shows slightly warmer and drier profiles over the urban area. But the profile of cloud water mixing ratio over the urban area in case URB is much larger. The diurnal cycles of cloud water mixing ratio and cloud cover fraction are examined in Figure 7. Large fluctuations of cloud cover fraction over the urban area are observed in case URB. We note that the fluctuations become smoother but do not completely disappear when longer averaging periods are used. This might be related to feedbacks between clouds, short-wave radiation and surface sensible heat flux. As the cloud cover and rainfall rate are enhanced due to the higher sensible heat flux, the short-wave radiation in the urban area is reduced, which then reduces the surface temperature and weakens the urban–rural circulation and convective activities in the urban area.

Figure 8(a) shows the domain-averaged diurnal cycles of surface precipitation rate. Again, the domain-averaged rainfall rates are similar between cases CTL and URB (Figure 8(a)). However, the average rainfall rate over the urban area is very different between the cases with an urban island (case URB) and the control case where there is no urban island. In particular, the rainfall rate (6.32 mm day^{-1}) over the urban area in the case URB is significantly larger than the rainfall rate (2.08 mm) in the control case. The surface precipitation rate also shows fluctuations over the diurnal cycle, and it seems that a period of 7 days is not sufficient to provide a smooth diurnal cycle of surface precipitation either. We also present the spatial distributions of surface precipitation at a few times on the last day (see red circles in Figure 8(b)) in Figure 9. It is clear that most of the precipitation

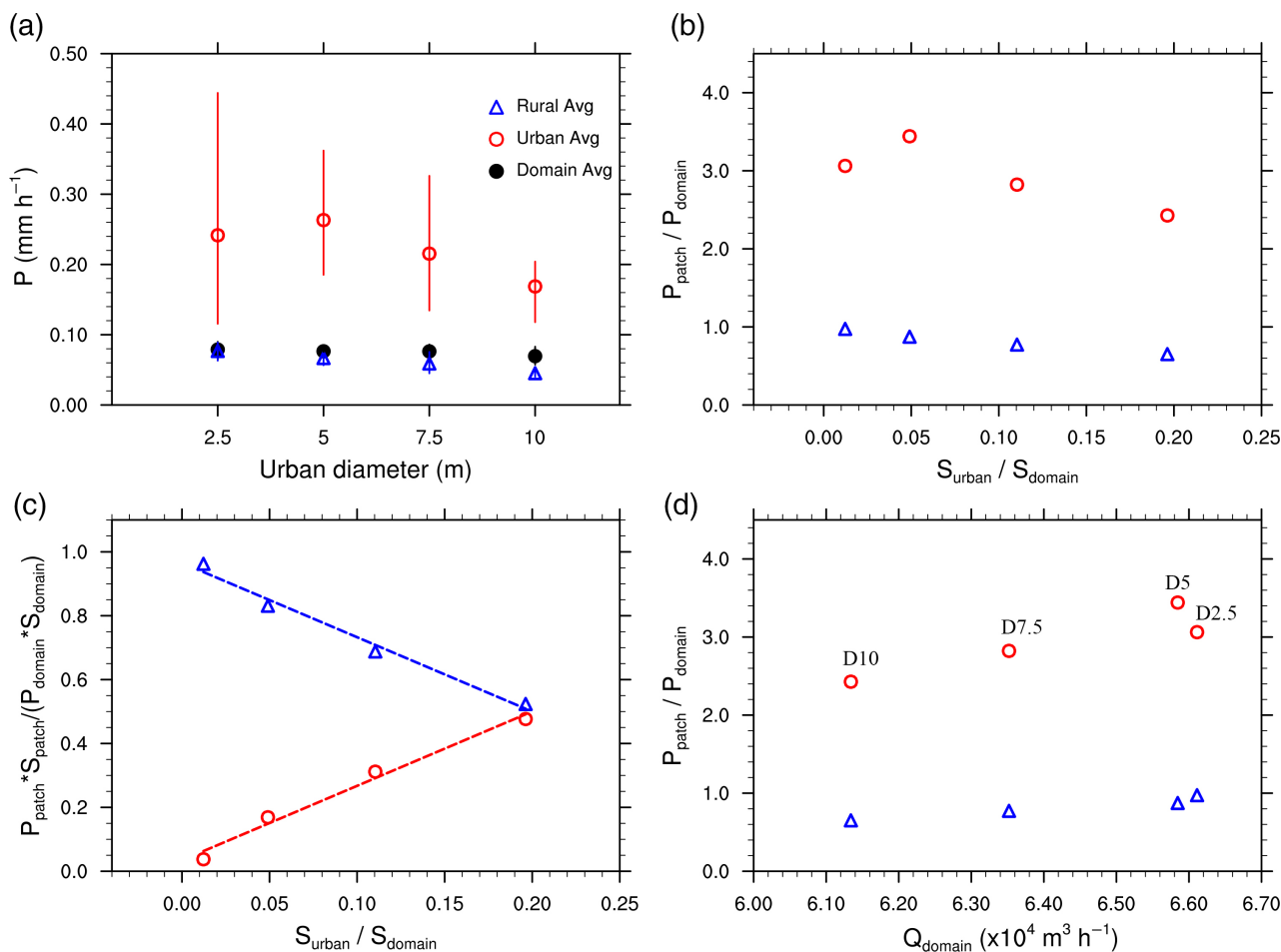


Figure 14. (a), (b) and (c) are the same as Figure 11 but for cases within different urban diameters in the domain. (d) is the relationship between the normalized rainfall rates and the total water supply from land. [Colour figure can be viewed at wileyonlinelibrary.com].

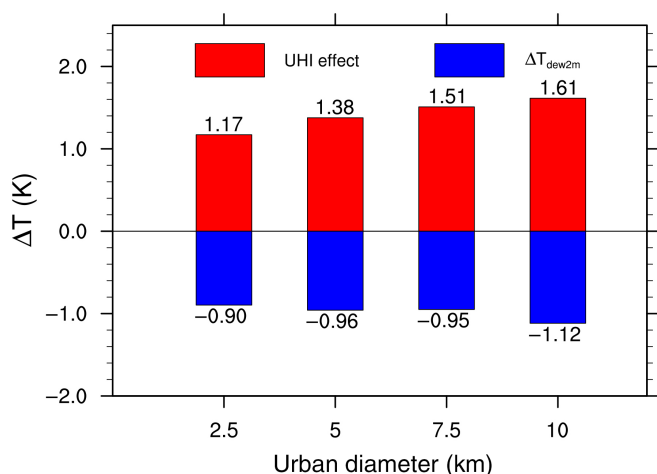


Figure 15. Same as Figure 12 but for cases within different urban diameters (km) in the domain. [Colour figure can be viewed at wileyonlinelibrary.com].

concentrates over the urban area indicated by the black circle. Rain prefers to occur over the urban area not only when the rainfall rate is the largest but also at the beginning and the ending of the event. We have also calculated the averaged results over the last 3, 5, 7 and 20 days and found that rain consistently prefers to occur over the urban area. This is consistent with the higher sensible heat flux in the urban area shown in Figure 5, which results in the urban heat island circulation and strong vertical motions over urban areas (Figure 9) and creates convergence zones in the urban area that facilitate convection. Previous studies also showed that clouds and rainfall tend to form sooner in the warmer area than the colder area (Kang and Bryan, 2011; Taylor *et al.*, 2011; Guillod *et al.*, 2015).

3.3. Impacts of the rural soil moisture

In this section, we examine the role of rural soil moisture in modulating the impact of an urban island on convection. Figure 10 shows the mean surface precipitation rates from four different cases in which the initial rural soil moisture varies. Visually it is clear that the existence of an urban island in the domain always leads to more rainfall in the urban area. The daily mean precipitation amounts range from smaller than 0.01 mm h^{-1} in the rural area to larger than 1 mm h^{-1} in the urban area.

Figure 11 provides further information about the scaling of changes in surface precipitation with respect to changes in soil moisture. As can be seen from Figure 11(a), the rainfall rates in all regions increase as the rural land becomes wetter. However, the increase in the urban rainfall rate is much stronger. When normalized by the domain-average precipitation rate, the contrast between urban and rural becomes even stronger. The normalized urban precipitation rate increases but the normalized rural precipitation rate decreases nearly linearly as the rural soil moisture increases. Figure 11(c) shows the total surface rainfall amounts normalized by the domain total rainfall amount. As can be seen, despite the precipitation rate being much higher in the urban area, due to its small fraction, it still receives far less precipitation than the rural area. Similar trends with increasing rural soil moisture are observed.

Figure 11 shows a strong positive relation between the rural land soil moisture and the urban rainfall rate and amount, but a negative feedback in terms of land–atmosphere coupling: the drier the urban area compared to the rural area, the more rainfall it receives. The negative feedback is consistent with a recent study focusing on soil moisture–precipitation coupling over heterogeneous terrain (Guillod *et al.*, 2015). To explore this further, the UHI effect and the moisture deficit effect are shown

in Figure 12 (Schmid and Niyogi, 2013). From Figure 12, the average UHI effects, defined as the difference in the 2 m potential temperature between the urban area and the rural area, are all higher than 1.0 K. We see a decrease of UHI effects as the initial soil gets wetter. This is because stronger rain events occurring over the urban area reduce the net surface radiation (Figure 5(b)). This suggests that the UHI effect is not responsible for the increasing trend with rural soil moisture as seen in Figure 11. The moisture deficit represented by the difference in the 2 m dew-point temperature, on the other hand, becomes larger with increasing rural soil moisture. A stronger moisture deficit effect, namely, a stronger gradient in atmospheric water vapour, creates a stronger moisture flux into the urban area from the rural area, which enhances the rainfall rate over the urban area.

3.4. Impacts of the urban size

In order to investigate the role of the urban size, we describe the results of cases within different urban sizes in this section. The same initial soil moisture as the URB case and CTL case is used. Figure 13 shows the spatial distributions of surface precipitation rates in different cases (D2.5, D5, D7.5 and D10). Case D2.5 where the urban island only occupies 1% of the domain starts to show an enhancement of rainfall rate around the urban area. However, unlike other cases, there are still places in the rural area with a comparable surface precipitation rate, and the maximum rainfall rate occurs at the edge between urban and rural areas. As the urban island expands, the rainfall concentrates more in the urban area and the rainfall rate becomes larger. For example, in cases D5 and D7.5 heavy rainfall rates are observed in urban areas. Interestingly, in the case D10, the rainfall rate in the urban area is much smaller than that in cases D5 and 7.5. This decrease is explained later.

When the rural area increases in the experiment while the urban area is maintained the same (cf. Figures 13(b) and (e)), the intensity of rainfall over the urban area does not change much ($0.262 \text{ mm day}^{-1}$ vs. $0.263 \text{ mm day}^{-1}$), despite the average rainfall rate over the domain increasing from 0.076 to 0.1 mm day^{-1} due to an enhanced water supply from a larger rural area.

To explain the results in Figure 13, Figure 14 shows the relation between surface precipitation and the urban island size. Specifically, Figure 14(a) shows the rainfall rates averaged over different regions; Figure 14(b) shows the urban/rural rainfall rates normalized by the domain-averaged rainfall rate; Figure 14(c) shows the urban/rural total rainfall amounts normalized by the domain total rainfall amount; Figure 14(d) shows the relationship between the normalized rainfall rates and the total water amount supplied by the land surface. Comparing Figures 14(a) and (c) shows that the trends in terms of rainfall rates and rainfall amounts become different since the size of the urban area changes. As expected, the fraction of total rainfall amount received by the urban area is increased due to the growing size of the urban area. The rainfall rate increases when the urban size increases from D2.5 to D5 but decreases with increasing urban size for urban sizes larger than D5. The large decrease in the urban rainfall rate in case D10 is because as the urban island expands (in case D10 the urban island occupies 20% of the domain), the water supply, which is almost entirely controlled by the rural area, is reduced. It is important to point out that although we have ensured the same initial available water in these cases, the total water supplied by the land surface still decreases as urban area increases (Figure 14(d)). This reduction in the water supply becomes a more severe constraint on the urban rainfall rate, despite the urban area still producing larger sensible heating and stronger vertical motions. This suggests that there exists an 'optimal' urban size, at least in this particular modelling framework, at which the urban rainfall rate is maximized. The existence of an 'optimal' or 'critical' size is consistent with previous study results (Schmid and Niyogi, 2013; Cronin *et al.*, 2015), although the exact value is different due to the difference in the modelling strategies.

Figure 15 further shows the average UHI intensity and moisture deficit effect. The average UHI intensity increases from 1.17 K in case D2.5 to 1.61 K in case D10. On the other hand, the moisture deficit effect represented by the difference in the 2 m dew-point temperature also become stronger when the urban area increases due to the enhanced rural soil moisture as the urban size increases. Considering changes in these two factors (i.e. a larger UHI effect and a similar moisture deficit effect for a larger urban island), one would think that the urban rainfall rate would be enhanced. However, Figure 14 shows that this only occurs when the urban size is smaller than a threshold, after which the reduction in the total water supply becomes more important and constrains the growth of urban rainfall rate.

4. Conclusion

In order to understand the impact of an urban island on precipitation, which is controlled by complex interactions between land and atmospheric processes, we develop an idealized framework using large-eddy simulations within the Weather Research and Forecasting model. Using this idealized framework, we also study how the effects of an urban island on precipitation are modulated by different rural soil moisture and different urban island sizes.

The urban area significantly affects the surface energy balance. The sensible heat flux in the urban area is much larger than the rural area, resulting in urban heat island circulations and stronger vertical motions. These changes further have an important effect on the distribution of surface precipitation. Compared to the control case where the whole domain is covered by grassland, the existence of an urban island results in a significantly larger rainfall rate (6.32 mm day^{-1} over the urban area in case URB compared to 2.06 mm day^{-1} in case CTL).

The cases with increasing rural soil moisture show increases in the urban and rural precipitation rates. The increases are almost linear, at least for the cases studied here. Although the UHI effects decrease as the rural soil moisture increases, most of the extra water supply from the wetter rural land is transported into the urban area. Under the influence of a stronger moisture deficit and thus a stronger moisture inflow, the urban precipitation rate and amount increase.

When the urban area gets larger but the initial available water remains the same, the UHI effect and the moisture deficit increases, but the water supply averaged over the whole simulation period decreases. This leads to an interesting phenomenon: as the urban size increases, the urban rainfall rate increases first and then decreases. This suggests that there is an 'optimal' scale at which the urban rainfall rate is maximized, at least in our modelling framework. Our simulations further suggest that this optimal scale occurs when the urban fraction lies between 1% and 10% of the domain.

In conclusion, the study is the first step towards understanding the influence of cities on moist convection in an idealized framework. This idealized framework offers a new way to understanding interactions between urban islands and other complexities such as the large-scale forcing, topography, and land–sea/land–lake boundaries, which are not considered here but will be systematically included in future investigations. In particular, because of the lack of large-scale forcing and the long memory of soil, our simulations have not reached radiative–convective equilibrium. However, the changes from day to day are small enough to justify an investigation of the behaviour of the system. Our modelling framework can be also used to study the broader research question of land–atmosphere coupling over heterogeneous terrain.

Acknowledgements

This work was supported by NSFC (51679119 and 91647107), and by Open Research Fund Program of State Key Laboratory

of Hydrosience and Engineering (sklhse-2015-A-02 and sklhse-2017-A-01). The simulations were performed on the Tianhe-2 National Supercomputer Center in Guangzhou. XZ acknowledges the support from the Tsinghua Scholarship for Overseas Graduate Studies. The data for this article are available through request to the corresponding author.

Appendix

Sensitivity to physical schemes and spatial resolutions

To investigate how physical schemes and domain resolutions affect our results, we use the Smagorinsky first-order subgrid-scale scheme in the case SGS and the WSM 3-class microphysical scheme in the case MP. To test the impact of the model resolution, we set the horizontal resolution to 50 m in the case H50, 200 m in the case H200 and set 50 levels in the vertical direction in case V50. In all these sensitivity simulations, the land surface is homogeneous as in the CTL case. All these cases just run for 2 weeks and the average results from the last 3 days are presented here.

Figure A1 shows the diurnal cycles of surface net radiation, surface sensible heat flux and latent heat flux. It can be seen from Figure A1 that there are no significant differences between the sensitivity experiments and the control experiment. Case MP shows a slightly smaller surface net radiation than case CTL. Some fluctuations of net radiation are observed in the sensitivity cases with different horizontal/vertical resolutions around 0900 LST. Clouds begin to form around this time (can be seen in Figure 3(a)) and changing the model resolution appears to affect the formation and amount of clouds. The fluctuations in the net radiation result in small changes in the surface sensible heat flux and latent heat flux.

Figure A2 shows the domain-averaged vertical profiles of potential temperature, water vapour mixing ratio and cloud water mixing ratio. It can be seen from Figures A2(a)–(c) that there is no significant difference between case SGS and the control case where the only difference is the subgrid-scale turbulence closure. However, changing the microphysical scheme (case MP) results in larger departures from the control simulation. In particular, using the WSM 3-class scheme in case MP generates a colder and drier atmosphere, mainly because ice and snow processes are simplified

in this scheme (Hong *et al.*, 2004; Hong and Lim, 2006). The WSM 6-class scheme is suitable for high-resolution simulations and can also take account of ice, snow and graupel processes. Details of the advantages of the WSM 6-class scheme have been documented elsewhere (Hong and Lim, 2006). Regarding the influence of horizontal and vertical resolutions (Figures A2(d) and (e)), a slightly colder and drier atmosphere is observed with an increased horizontal resolution. Figure A2(f) shows the profiles of cloud water mixing ratio, and the cases with coarser resolutions have smaller values.

Figure A3 then examines diurnal cycles of cloud water mixing ratio and cloud cover fraction. We can see similar diurnal cycles of cloud cover fraction (i.e. the ratio of cloud coverage area to domain size) indicated by the solid black line and cloud water mixing ratio indicated by the shading across all cases but MP. With a colder and drier atmosphere generated in the case MP (Figures A2(a) and (b)), the maximum cloud height is capped at 4 km, which then reduces the total rainfall amount. Besides this, a higher cloud cover fraction in case MP is noticed. Due to the limitation of the maximum cloud height and cloud amount, most of the shallow convection indicated by the large cloud fraction over the domain does not develop into deep convection and there is no more rain in case MP compared with case CTL (as will be seen in Figure A6). Coarse horizontal and vertical resolution both show smaller cloud water mixing ratio than case CTL, but the diurnal cycle and the cloud height are similar to the case CTL. We note that clouds in case V50 start to develop later than in the other cases (Figure A3(c)). The delay of clouds and rainfall is probably related to the sensitivity of the microphysical scheme to the vertical resolution (Hong and Lim, 2006).

Figure A4 shows the resolved turbulent kinetic energy (TKE) and its three components at 1200 LST. The resolved TKE is defined as:

$$TKE = \frac{1}{2}(\langle u'u' \rangle + \langle v'v' \rangle + \langle w'w' \rangle), \quad (\text{A1})$$

where u , v and w are longitudinal, meridional and vertical velocities, respectively. The angle brackets and primes denote plane averages and fluctuations, respectively. Because the resolution is coarse near the top of the domain and the TKE in the free atmosphere should not be large, the profiles of TKE are only drawn from the ground to the height of 2 km (Figure A4). It

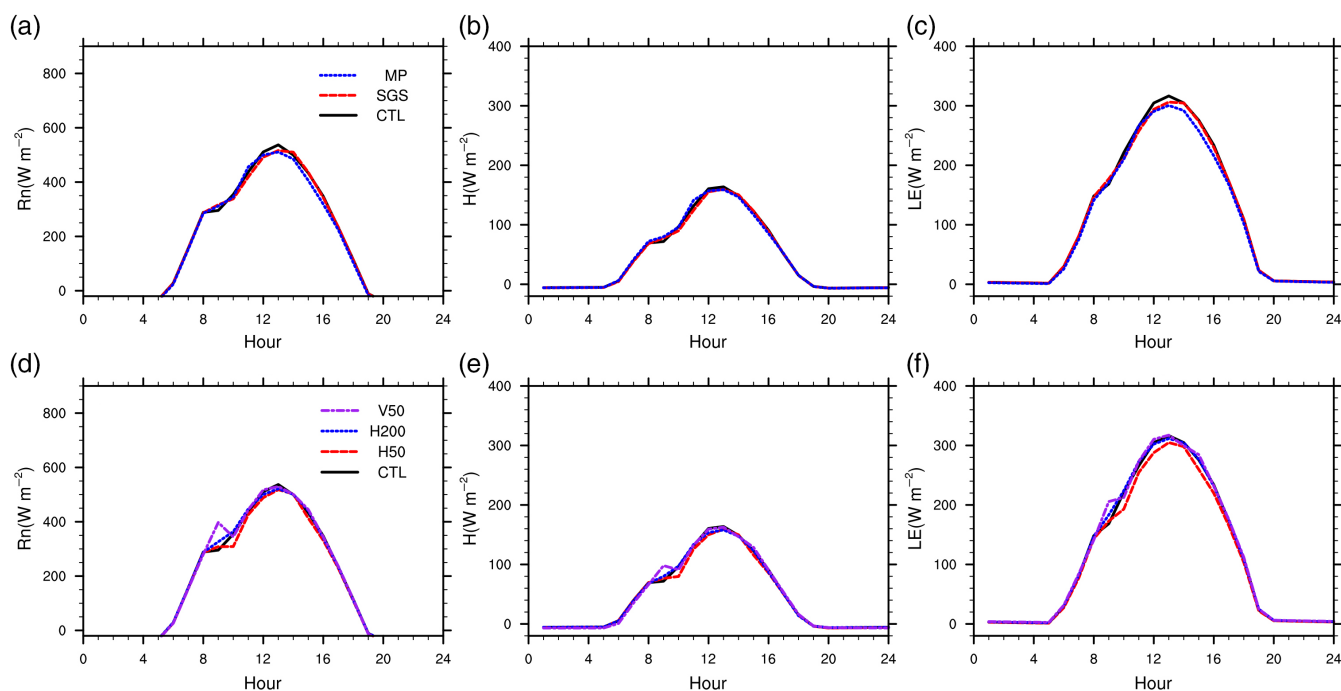


Figure A1. The average diurnal cycle of (a, d) surface net radiation (Rn), (b, e) surface sensible heat flux (H) and (c, f) surface latent heat flux (LE), for CTL and five experiments. [Colour figure can be viewed at wileyonlinelibrary.com].

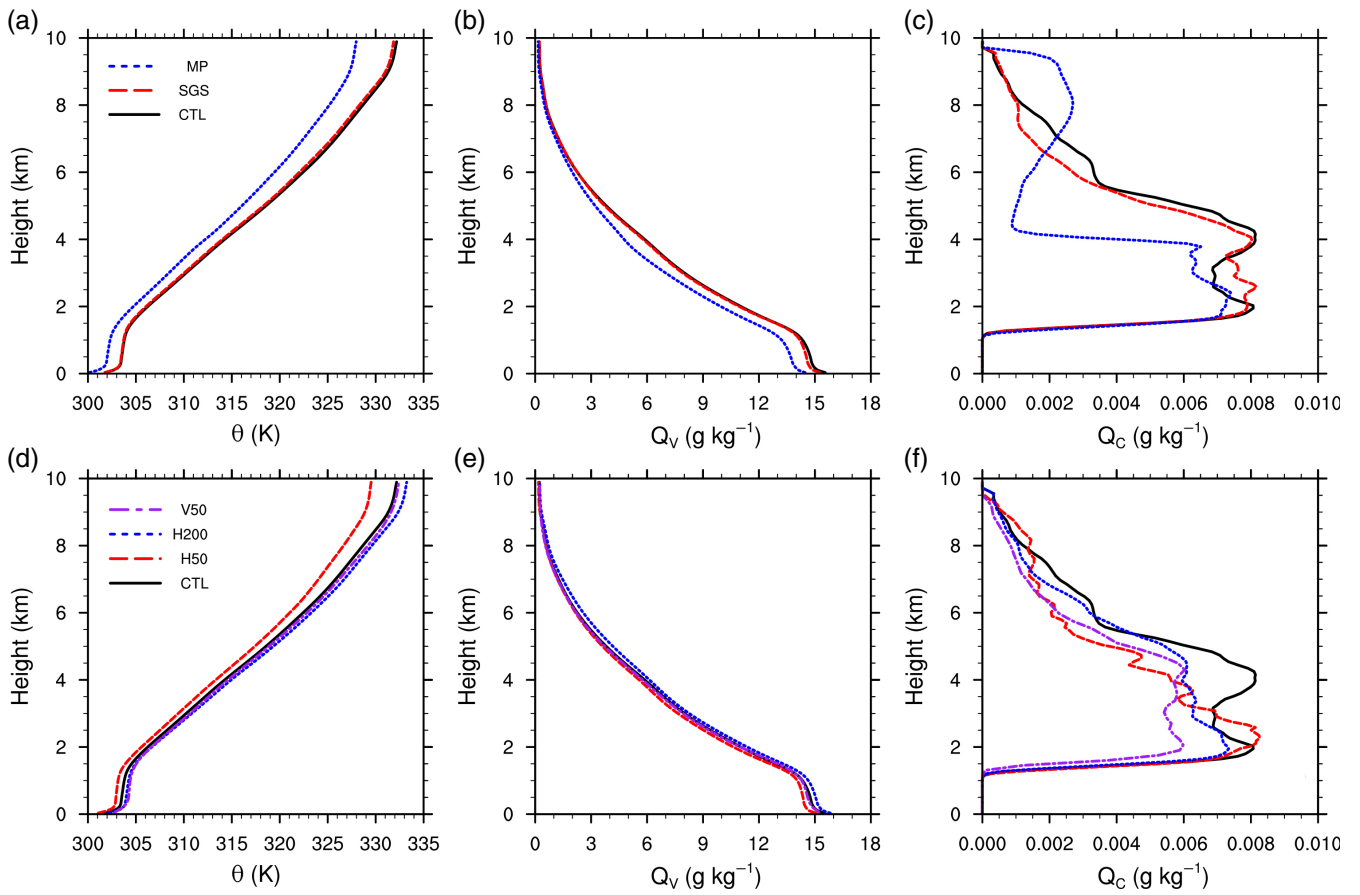


Figure A2. Vertical profiles of domain-averaged (a, d) potential temperature (K), (b, e) water vapour mixing ratio ($g\ kg^{-1}$), and (c, f) cloud water mixing ratio ($g\ kg^{-1}$), for CTL and five experiments. [Colour figure can be viewed at wileyonlinelibrary.com].

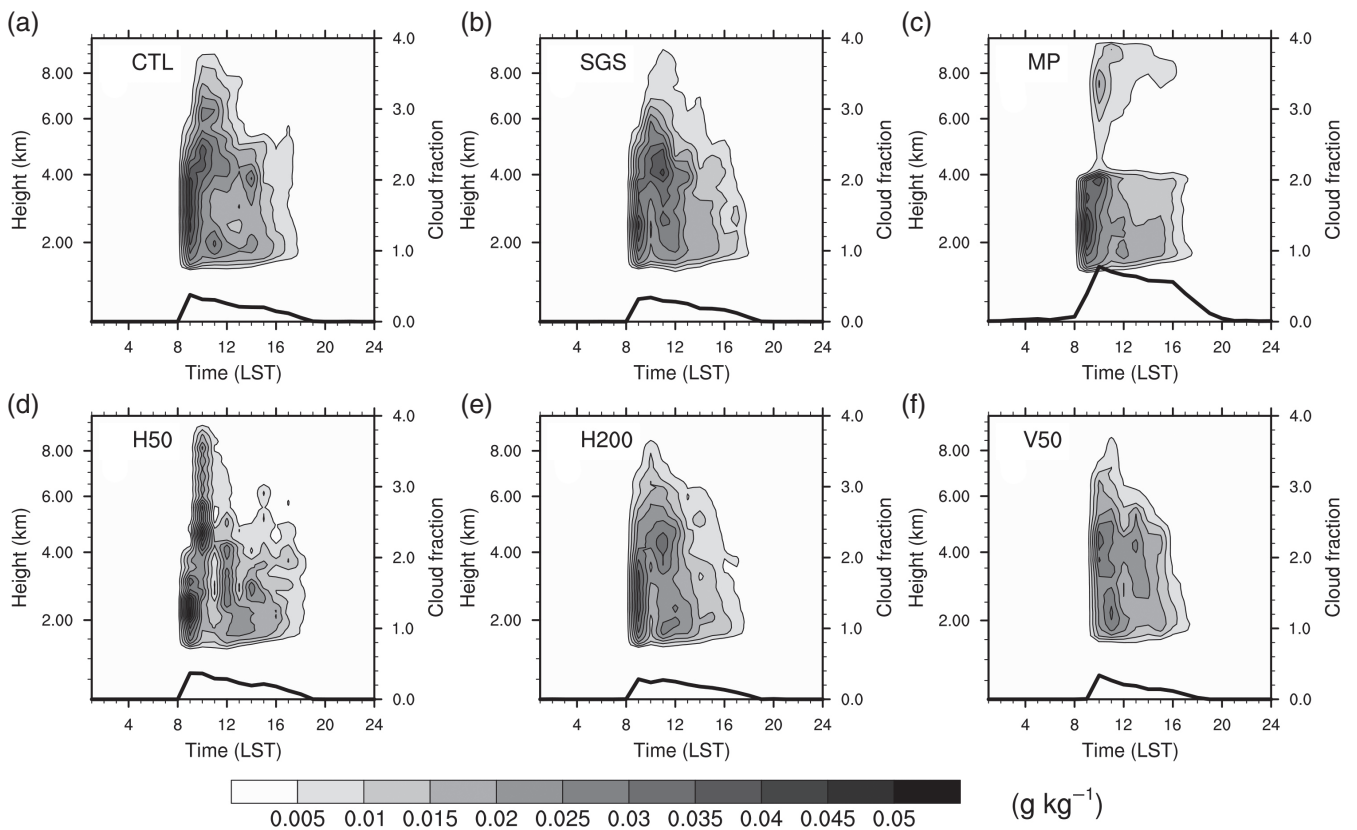


Figure A3. The diurnal cycle of cloud water mixing ratio ($g\ kg^{-1}$, shaded area) and cloud cover fraction (solid black line). The (a), (b), (c), (d), (e) and (f) are results of the cases CTL, SGS, MP, H50, H200 and V50, respectively. Note that the y-axis is not equidistant as the WRF model uses eta levels in the vertical direction.

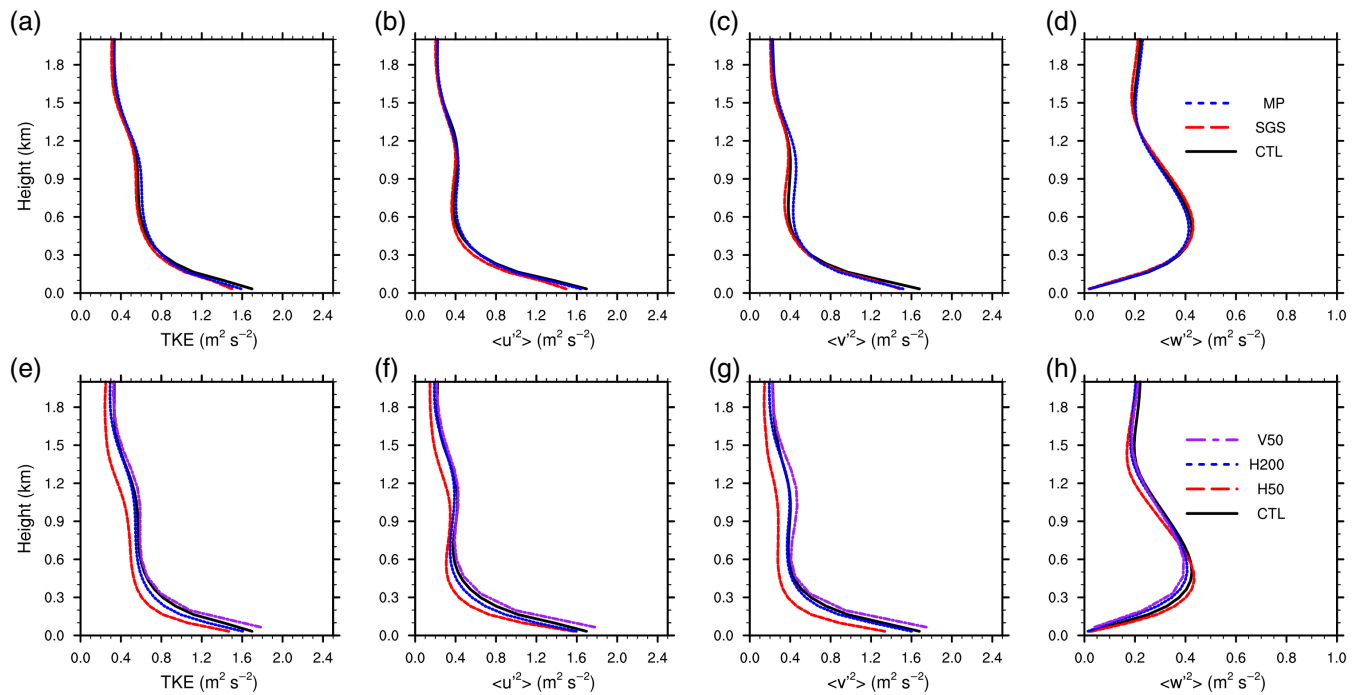


Figure A4. Vertical profiles of TKE and its three components: (a, e) TKE; (b, f) $\langle u'u' \rangle$; (c, g) $\langle v'v' \rangle$; (d, h) $\langle w'w' \rangle$. (a–d) compare cases MP, SGS and CTL, while (e–h) show cases V50, H200, H50 and CTL. [Colour figure can be viewed at wileyonlinelibrary.com].

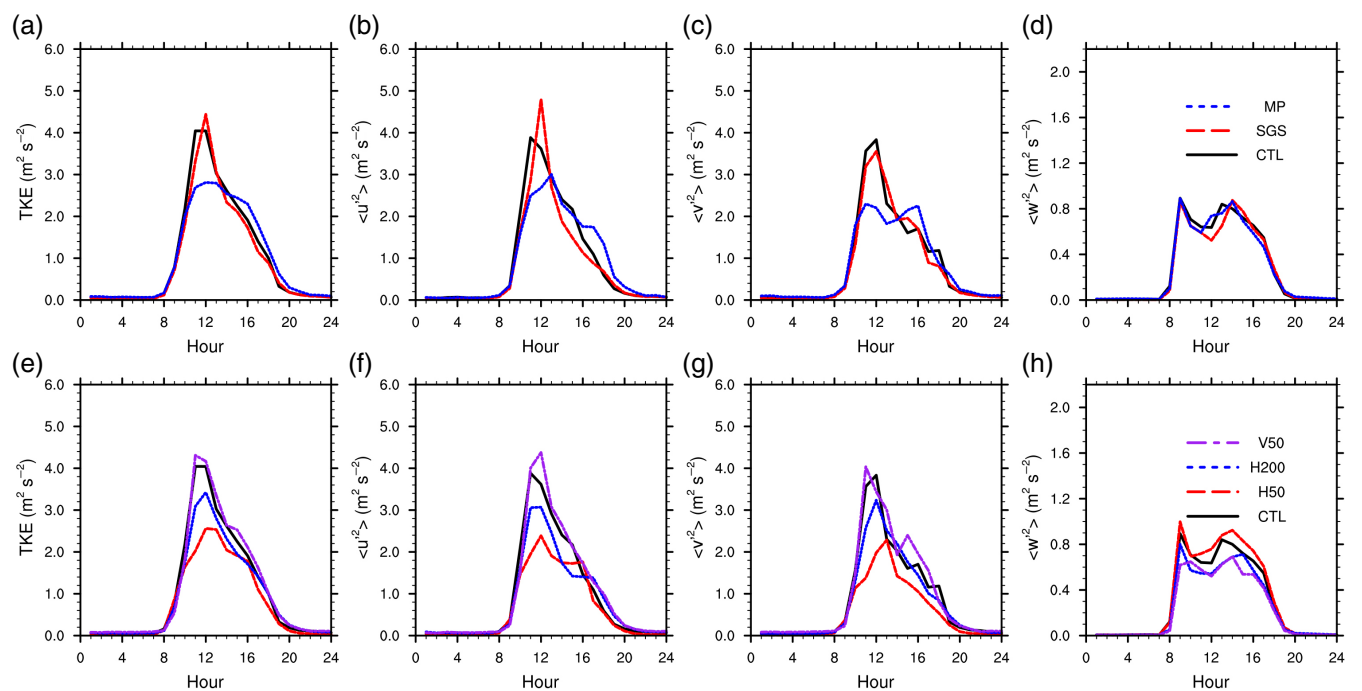


Figure A5. Same as Figure A4 but for the average diurnal cycle of TKE and its three components at a height of 200 m. [Colour figure can be viewed at wileyonlinelibrary.com].

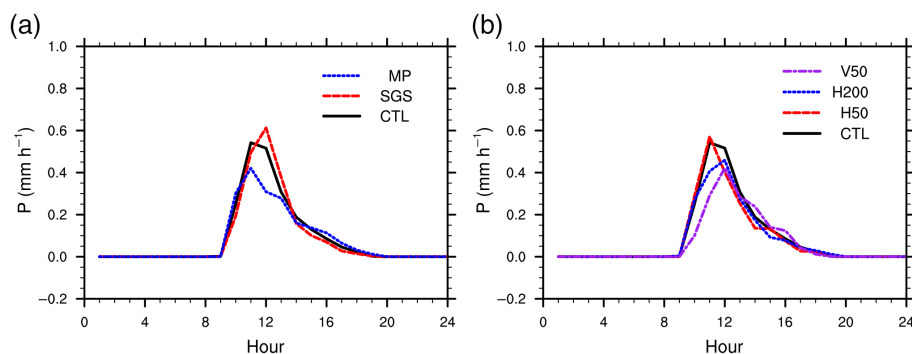


Figure A6. (a, b) The average diurnal cycle of surface precipitation rate P (mm h^{-1}), for CTL and five experiments. [Colour figure can be viewed at wileyonlinelibrary.com].

can be seen that the average vertical profiles of TKE and its three components are very similar among different cases. TKE near the ground shows a relatively larger difference than the upper atmosphere. Then Figure A5 examines diurnal cycles of TKE and its three components at a height of 200 m. For the diurnal cycles, it can be seen more clearly that the changes in the TKE are mostly due to the horizontal components as longitudinal, meridional and vertical $\langle w'w' \rangle$ is small. Case SGS shows a similar diurnal cycle with case CTL. The subgrid scheme used in the case SGS is the Smagorinsky scheme, which is different from the case CTL, and in principle may alter the TKE below the subgrid-scale. Since the TKE in Figures A4 and A5 represent the resolved TKE but not the subgrid-scale TKE, it is clear that the subgrid scheme has insignificant impacts on the resolved TKE. For the case MP, the different cloud density and cloud cover fraction (Figure A3(c)) reduce the net surface net radiation (Figure A1(a)) and affect the development of TKE around noon (Figure A5(a)). But the average value (Figure A4(a)) over the daytime is still close to case CTL. In terms of the effect of resolutions, the vertical resolution has little impact on the TKE. We also notice different amplitudes of the three components of TKE. The $\langle w'w' \rangle$ in case H200 and case V50 show slightly smaller values, while it is slightly larger in case H50. The differences among horizontal components are larger. The finest case H50 generates the smallest TKE while cases H200 and CTL are more similar, suggesting a stronger sensitivity to horizontal resolution than vertical resolution. This is consistent with previous studies (Talbot *et al.*, 2012).

Figure A6 shows the diurnal cycle of surface precipitation. In Figure A1, the surface evapotranspiration rates are similar in these sensitivity cases, while the surface precipitation has similar diurnal cycles but with different amplitudes. The daily average rainfall amounts of different cases are: 2.09 mm day⁻¹ (case CTL), 2.05 mm day⁻¹ (case SGS), 1.83 mm day⁻¹ (case MP), 1.91 mm day⁻¹ (case X50), 1.85 mm day⁻¹ (case H200) and 1.65 mm day⁻¹ (case V50). Case V50 with a coarser vertical resolution generates the smallest value. The beginning, the development and the end of the rainfall event are almost the same.

According to these sensitivity experiment results, it can be generalized that different physical schemes and spatial resolutions have relatively small influences on the surface energy balance and vertical profiles of domain-averaged atmospheric properties. The microphysical scheme seems to play a more important role in controlling the cloud water distribution than the subgrid-scale turbulence closure and the grid resolution. The surface precipitation is more sensitive to the vertical resolution than the horizontal resolution, whereas the resolved TKE is more sensitive to the horizontal resolution than the vertical resolution.

References

- Arnfield AJ. 2003. Two decades of urban climate research: A review of turbulence, exchanges of energy and water, and the urban heat island. *Int. J. Climatol.* **23**: 1–26. <https://doi.org/10.1002/joc.859>.
- Betts AK, Ball JH, Beljaars ACM, Miller MJ, Viterbo PA. 1996. The land surface–atmosphere interaction: A review based on observational and global modeling perspectives. *J. Geophys. Res.* **101**: 7209–7225. <https://doi.org/10.1029/95JD02135>.
- Changnon SA Jr. 1981. *METROMEX: A Review and Summary*. American Meteorological Society: Boston, MA.
- Changnon SA Jr, Huff FA, Semonin RG. 1971. METROMEX: An investigation of inadvertent weather modification. *Bull. Am. Meteorol. Soc.* **52**: 958–968. [https://doi.org/10.1175/1520-0477\(1971\)052<0958:MAIOIW>2.0.CO;2](https://doi.org/10.1175/1520-0477(1971)052<0958:MAIOIW>2.0.CO;2).
- Cronin TW, Emanuel KA, Molnar P. 2015. Island precipitation enhancement and the diurnal cycle in radiative-convective equilibrium. *Q. J. R. Meteorol. Soc.* **141**: 1017–1034. <https://doi.org/10.1002/qj.2443>.
- Deardorff JW. 1980. Stratocumulus-capped mixed layers derived from a three-dimensional model. *Boundary-Layer Meteorol.* **18**: 495–527. <https://doi.org/10.1007/BF00119502>.
- Dudhia J. 1989. Numerical study of convection observed during the winter monsoon experiment using a meso-scale two-dimensional model. *J. Atmos. Sci.* **46**: 3077–3107. [https://doi.org/10.1175/1520-0469\(1989\)046<3077:NSOCOD>2.0.CO;2](https://doi.org/10.1175/1520-0469(1989)046<3077:NSOCOD>2.0.CO;2).
- Eltahir EA. 1998. A soil moisture–rainfall feedback mechanism: 1. Theory and observations. *Water Resour. Res.* **34**: 765–776. <https://doi.org/10.1029/97WR03499>.
- Findell KL, Eltahir EAB. 2003. Atmospheric controls on soil moisture–boundary layer interactions. Part I: Framework development. *J. Hydrometeorol.* **4**: 552–569. [https://doi.org/10.1175/1525-7541\(2003\)004<0552:ACOSML>2.0.CO;2](https://doi.org/10.1175/1525-7541(2003)004<0552:ACOSML>2.0.CO;2).
- Gentine P, Holtslag AAM, D'Andrea F, Ek M. 2013. Surface and atmospheric controls on the onset of moist convection over land. *J. Hydrometeorol.* **14**: 1443–1462. <https://doi.org/10.1175/JHM-D-12-0137.1>.
- Grimm NB, Faeth SH, Golubiewski NE, Redman CL, Wu J, Bai X, Briggs JM. 2008. Global change and the ecology of cities. *Science* **319**: 756–760. <https://doi.org/10.1126/science.1150195>.
- Grimmond S. 2007. Urbanization and global environmental change: Local effects of urban warming. *Geogr. J.* **173**: 83–88. https://doi.org/10.1111/j.1475-4959.2007.232_3.x.
- Guilod BP, Orłowsky B, Miralles DG, Teuling AJ, Seneviratne SI. 2015. Reconciling spatial and temporal soil moisture effects on afternoon rainfall. *Nat. Commun.* **6**: 6443. <https://doi.org/10.1038/ncomms7443>.
- Haiden T. 1997. An analytical study of cumulus onset. *Q. J. R. Meteorol. Soc.* **123**: 1945–1960. <https://doi.org/10.1002/qj.49712354309>.
- Hohenegger C, Brockhaus P, Bretherton CS, Schär C. 2009. The soil moisture–precipitation feedback in simulations with explicit and parameterized convection. *J. Clim.* **22**: 5003–5020. <https://doi.org/10.1175/2009JCLI2604.1>.
- Hong S, Lim JJ. 2006. The WRF single-moment 6-class microphysics scheme (WSM6). *J. Korean Meteorol. Soc.* **42**: 129–151.
- Hong SY, Dudhia J, Chen SH. 2004. A revised approach to ice microphysical processes for the bulk parameterization of clouds and precipitation. *Mon. Weather Rev.* **132**: 103–120. [https://doi.org/10.1175/1520-0493\(2004\)132<0103:ARATIM>2.0.CO;2](https://doi.org/10.1175/1520-0493(2004)132<0103:ARATIM>2.0.CO;2).
- Juang J, Porporato A, Stoy PC, Siqueira MS, Oishi AC, Detto M, Kim H, Katul GG. 2007. Hydrologic and atmospheric controls on initiation of convective precipitation events. *Water Resour. Res.* **43**: W03421. <https://doi.org/10.1029/2006WR004954>.
- Kang S, Bryan GH. 2011. A large-eddy simulation study of moist convection initiation over heterogeneous surface fluxes. *Mon. Weather Rev.* **139**: 2901–2917. <https://doi.org/10.1175/MWR-D-10-05037.1>.
- Kang S, Lenschow DH. 2014. Temporal evolution of low-level winds induced by two-dimensional mesoscale surface heat-flux heterogeneity. *Boundary-Layer Meteorol.* **151**: 501–529. <https://doi.org/10.1007/s10546-014-9912-8>.
- Koster RD, Suarez MJ. 2001. Soil moisture memory in climate models. *J. Hydrometeorol.* **2**: 558–570. [https://doi.org/10.1175/1525-7541\(2001\)002<0558:SMMICM>2.0.CO;2](https://doi.org/10.1175/1525-7541(2001)002<0558:SMMICM>2.0.CO;2).
- Lei M, Niyogi D, Kishitawal C, Pielke RAS, Beltran-Przekurat A, Nobis TE, Vaidya SS. 2008. Effect of explicit urban land surface representation on the simulation of the 26 July 2005 heavy rain event over Mumbai, India. *Atmos. Chem. Phys.* **8**: 5975–5995. <https://doi.org/10.5194/acp-8-5975-2008>.
- Liu G, Sun J, Yin L. 2011. Turbulence characteristics of the shear-free convective boundary layer driven by heterogeneous surface heating. *Boundary-Layer Meteorol.* **140**: 57–71. <https://doi.org/10.1007/s10546-011-9591-7>.
- Lowry WP. 1998. Urban effects on precipitation amount. *Prog. Phys. Geog.* **22**: 477–520. <https://doi.org/10.1177/030913339802200403>.
- Mahmood R, Pielke RA, Hubbard KG, Niyogi D, Dirmeyer PA, McAlpine C, Carleton AM, Hale R, Gameda S, Beltrán Przekurat A. 2014. Land cover changes and their biogeophysical effects on climate. *Int. J. Climatol.* **34**: 929–953. <https://doi.org/10.1002/joc.3736>.
- Mlawer EJ, Taubman SJ, Brown PD, Iacono MJ, Clough SA. 1997. Radiative transfer for inhomogeneous atmospheres: RRTM, a validated correlated-k model for the longwave. *J. Geophys. Res.* **102**: 16663–16682. <https://doi.org/10.1029/97JD00237>.
- Moeng C, Dudhia J, Klemp J, Sullivan P. 2007. Examining two-way grid nesting for large eddy simulation of the PBL using the WRF model. *Mon. Weather Rev.* **135**: 2295–2311. <https://doi.org/10.1002/joc.3736>.
- Nie W, Sun T, Ni G. 2014. Spatiotemporal characteristics of anthropogenic heat in an urban environment: A case study of Tsinghua Campus. *Build. Environ.* **82**: 675–686. <https://doi.org/10.1016/j.buildenv.2014.10.011>.
- Nie W, Zaitchik BF, Ni G, Sun T. 2017. Impacts of anthropogenic heat on summertime rainfall in Beijing. *J. Hydrometeorol.* **18**: 693–712. <https://doi.org/10.1175/JHM-D-16-0173.1>.
- Oke TR. 1982. The energetic basis of the urban heat-island. *Q. J. R. Meteorol. Soc.* **108**: 1–24. <https://doi.org/10.1002/qj.4971084502>.
- Pielke RA Sr, Pitman A, Niyogi D, Mahmood R, McAlpine C, Hossain F, Goldewijk KK, Nair U, Betts R, Fall S, Reichstein M, Kabat P, de Noblet N. 2011. Land use/land cover changes and climate: modeling analysis and observational evidence. *Wiley Interdiscip. Rev.: Clim. Change* **2**: 828–850. <https://doi.org/10.1002/wcc.144>.
- Reinert D, Wirth V. 2009. A new large-eddy simulation model for simulating air flow and warm clouds above highly complex terrain. Part II: The moist model and its application to banner clouds. *Boundary-Layer Meteorol.* **133**: 113–136. <https://doi.org/10.1007/s10546-009-9419-x>.
- Rochetin N, Lintner BR, Findell KL, Sobel AH, Gentine P. 2014. Radiative-convective equilibrium over a land surface. *J. Clim.* **27**: 8611–8629. <https://doi.org/10.1175/JCLI-D-13-00654.1>.
- Santanello JA, Peters-Lidard CD, Kumar SV. 2011. Diagnosing the sensitivity of local land–atmosphere coupling via the soil moisture–boundary layer interaction. *J. Hydrometeorol.* **12**: 766–786. <https://doi.org/10.1175/JHM-D-10-05014.1>.

- Schlemmer L, Hohenegger C, Schmidli J, Bretherton CS, Schär C. 2011. An idealized cloud-resolving framework for the study of midlatitude diurnal convection over land. *J. Atmos. Sci.* **68**: 1041–1057. <https://doi.org/10.1175/2010JAS3640.1>.
- Schlemmer L, Hohenegger C, Schmidli J, Schär C. 2012. Diurnal equilibrium convection and land surface–atmosphere interactions in an idealized cloud-resolving model. *Q. J. R. Meteorol. Soc.* **138**: 1526–1539. <https://doi.org/10.1002/qj.1892>.
- Schmid PE, Niyogi D. 2013. Impact of city size on precipitation-modifying potential. *Geophys. Res. Lett.* **40**: 5263–5267. <https://doi.org/10.1002/grl.50656>.
- Seneviratne SI, Corti T, Davin EL, Hirschi M, Jaeger EB, Lehner I, Orlowsky B, Teuling AJ. 2010. Investigating soil moisture–climate interactions in a changing climate: A review. *Earth-Sci. Rev.* **99**: 125–161. <https://doi.org/10.1016/j.earscirev.2010.02.004>.
- Shepherd JM. 2005. A review of current investigations of urban-induced rainfall and recommendations for the future. *Earth Interact.* **9**: 1–27. <https://doi.org/10.1175/EI156.1>.
- Shepherd JM, Carter M, Manyin M, Messen D, Burian S. 2010. The impact of urbanization on current and future coastal precipitation: A case study for Houston. *Environ. Plann. B: Plann. Des.* **37**: 284–304. <https://doi.org/10.1068/b34102t>.
- Siqueira M, Katul G, Porporato A. 2009. Soil moisture feedbacks on convection triggers: the role of soil–plant hydrodynamics. *J. Hydrometeorol.* **10**: 96–112. <https://doi.org/10.1175/2008JHM1027.1>.
- Stull RB, Eloranta EW. 1984. Boundary layer experiment – 1983. *Bull. Am. Meteorol. Soc.* **65**: 450–456. [https://doi.org/10.1175/1520-0477\(1984\)065<0450:BLE>2.0.CO;2](https://doi.org/10.1175/1520-0477(1984)065<0450:BLE>2.0.CO;2).
- Talbot C, Bou-Zeid E, Smith J. 2012. Nested mesoscale large-eddy simulations with WRF: Performance in real test cases. *J. Hydrometeorol.* **13**: 1421–1441. <https://doi.org/10.1175/JHM-D-11-048.1>.
- Taylor CM, Gounou A, Guichard F, Harris PP, Ellis RJ, Couvreur F, De Kauwe M. 2011. Frequency of Sahelian storm initiation enhanced over mesoscale soil-moisture patterns. *Nat. Geosci.* **4**: 430–433. <https://doi.org/10.1038/ngeo1173>.
- Taylor CM, de Jeu RAM, Guichard F, Harris PP, Dorigo WA. 2012. Afternoon rain more likely over drier soils. *Nature* **489**: 423–426. <https://doi.org/10.1038/nature11377>.
- Trusilova K, Jung M, Churkina G, Karstens U, Heimann M, Claussen M. 2008. Urbanization impacts on the climate in Europe: numerical experiments by the PSU–NCAR mesoscale model (MM5). *J. Appl. Meteorol. Climatol.* **47**: 1442–1455. <https://doi.org/10.1175/2007JAMC1624.1>.
- Tuttle S, Salvucci G. 2016. Empirical evidence of contrasting soil moisture–precipitation feedbacks across the United States. *Science* **352**: 825. <https://doi.org/10.1126/science.aaa7185>.
- United Nations DOEA. 2014. ‘World urbanization prospects: The 2014 Revision’, Highlights (ST/ESA/SER.A/352).
- Wilde NP, Stull RB, Eloranta EW. 1985. The LCL zone and cumulus onset. *J. Clim. Appl. Meteorol.* **24**: 640–657. [https://doi.org/10.1175/1520-0450\(1985\)024<0640:TLZACO>2.0.CO;2](https://doi.org/10.1175/1520-0450(1985)024<0640:TLZACO>2.0.CO;2).
- Xu KM, Cederwall RT, Donner LJ, Grabowski WW, Guichard F, Johnson DE, Khairoutdinov M, Krueger SK, Petch JC, Randall DA, Seman CJ, Tao WK, Wang DH, Xie SC, Yio JJ, Zhang MH. 2002. An intercomparison of cloud-resolving models with the atmospheric radiation measurement summer 1997 intensive observation period data. *Q. J. R. Meteorol. Soc.* **128**: 593–624. <https://doi.org/10.1256/003590002321042117>.
- Yamaguchi T, Feingold G. 2012. Technical note: Large-eddy simulation of cloudy boundary layer with the advanced research WRF model. *J. Adv. Model. Earth Syst.* **4**: M09003. <https://doi.org/10.1029/2012MS000164>.
- Yang L, Smith JA, Baeck ML, Bou-Zeid E, Jessup SM, Tian F, Hu H. 2014. Impact of urbanization on heavy convective precipitation under strong large-scale forcing: a case study over the Milwaukee–Lake Michigan region. *J. Hydrometeorol.* **15**: 261–278. <https://doi.org/10.1175/JHM-D-13-020.1>.
- Yeung JK, Smith JA, Baeck ML, Villarini G. 2015. Lagrangian analyses of rainfall structure and evolution for organized thunderstorm systems in the urban corridor of the northeastern United States. *J. Hydrometeorol.* **16**: 1575–1595. <https://doi.org/10.1175/JHM-D-14-0095.1>.
- Yin J, Albertson JD, Rigby JR, Porporato A. 2015. Land and atmospheric controls on initiation and intensity of moist convection: CAPE dynamics and LCL crossings. *Water Resour. Res.* **51**: 8476–8493. <https://doi.org/10.1002/2015WR017286>.
- Zhang N, Wang X, Peng Z. 2014a. Large-eddy simulation of mesoscale circulations forced by inhomogeneous urban heat island. *Boundary-Layer Meteorol.* **151**: 179–194. <https://doi.org/10.1007/s10546-013-9879-x>.
- Zhang Y, Smith JA, Luo L, Wang Z, Baeck ML. 2014b. Urbanization and rainfall variability in the Beijing metropolitan region. *J. Hydrometeorol.* **15**: 2219–2235. <https://doi.org/10.1175/JHM-D-13-0180.1>.
- Zhu X, Ni G, Cong Z, Sun T, Li D. 2016. Impacts of surface heterogeneity on dry planetary boundary layers in an urban–rural setting. *J. Geophys. Res. Atmos.* **121**: 12164–12179. <https://doi.org/10.1002/2016JD024982>.